Chatterjee, Kuntal; Dopfer, Otto

Microhydration Structures of Protonated Oxazole

Chatterjee, K., & Dopfer, O. (2019). Microhydration Structures of Protonated Oxazole. The Journal of Physical Chemistry A. https://doi.org/10.1021/acs.jpca.9b06587

Microhydration Structures of Protonated Oxazole

Kuntal Chatterjee and Otto Dopfer*

Institut für Optik und Atomare Physik, TU Berlin, Hardenbergstr. 36, 10623 Berlin, Germany

* Corresponding author: dopfer@physik.tu-berlin.de

Abstract

The initial microhydration structures of the protonated pharmaceutical building block oxazole (Ox), H^+Ox-$W_{n\leq4}$, are determined by infrared photodissociation (IRPD) spectroscopy combined with quantum chemical dispersion-corrected density functional theory calculations (B3LYP-D3/aug-cc-pVTZ). Protonation of Ox, achieved by chemical ionization in an H_2-containing plasma, occurs at the most basic N atom. The analysis of systematic shifts of the NH and OH stretch vibrations as a function of the cluster size provides a clear picture for the preferred cluster growth in H^+Ox-W_n. For n=1-3, the IRPD spectra are dominated by a single isomer, and microhydration of H^+Ox with hydrophilic protic W ligands occurs by attachment of a hydrogen-bonded (H-bonded) W_n solvent cluster to the acidic NH group via NH…O H-bond. Such H-bonded networks are stabilized by strong cooperativity effects. This is in contrast to previously studied hydrophobic ligands, which prefer internal ion solvation. The strength of the NH…O ionic H-bond increases with the degree of hydration because of the increasing proton affinity (PA) of the W_n cluster. At n=4, proton-transferred structures of the type $Ox\text{-}H^+W_n$ become energetically competitive with H^+Ox-W_n structures, because differences in solvation energies can compensate for the differences in the PAs, and barrierless proton transfer from H^+Ox to the W_n solvent subcluster becomes feasible. Indeed, the IRPD spectrum of the n=4 cluster is more complex suggesting the presence of more than one isomer, although it lacks unequivocal evidence for the predicted intracluster proton transfer.

Revised version submitted to J. Phys. Chem. A on August 6 (2019)

1. Introduction

Hydration of biomolecules is a fundamental chemical process that regulates their stability, flexibility, and function. As a result, solvating water layers are nowadays considered as an integral part of such bioactive macromolecules.[1–10] The absence of water often leads to inactivity of proteins and nucleic acids. In general, biological macromolecules bind to the solvating surface water ligands (often called "biological" water) through extended hydrogen bonded (H-bonded) networks, which are pivotal to the recognition of various drugs and proteins.[11–16] Experimentally, a number of prudent techniques, including X-ray diffraction, nuclear magnetic resonance, and neutron scattering, have been employed in the condensed phase to understand the impact of hydration on the inherent physical and chemical properties of the bioactive species.[10] However, most of these strategies suffer from macroscopic solvent effects, interactions with other molecules and substrates, and thermal and heterogeneous broadening, which prevent the determination of intrinsic fundamental biochemical characteristics of such molecules and the structure and dynamics of individual water molecules in the first hydration layer.[10,17] These problems can be circumvented by interrogating individual molecules and clusters in the gas phase.[10,17–26] The spectroscopic study of mass-selected clusters in combination with high-level quantum chemical calculations provides detailed information about the intrinsic molecular properties of the solute molecules and their changes upon sequential addition of individual solvent molecules.

Herein, we address the microhydration of protonated oxazole (H^+Ox), which is an important biomolecular building block of numerous pharmaceutical and natural products, exhibiting antibiotic, antitumor, antituberculosis, antiinflammatory, and HIV-inhibitory properties.[27–36] Amino acids with an Ox nucleus are extensively used to modify the bioactivity of various macromolecules.[27,28,37–43] It is well established that the structure and reactivity of such molecules are often regulated by solvation, substitution, and protonation of the fundamental building blocks like Ox. For example, protonation of the Ox ring of the acetyl-coenzyme A carboxylase (ACCase) inhibitor, Metamifop, influences its binding efficiency with that particular enzyme.[44]

The structure and vibrations of neutral Ox in its planar ground electronic state have been explored by microwave, infrared (IR), and Raman spectroscopy, as well as quantum chemical calculations.[45–53] No experimental information is available for any cluster of Ox. Low-level calculations predict for the neutral Ox-water (Ox-W) dimer hydration at the N center of Ox via a OH…N H-bond, because the two lone pairs of the O atom of Ox participate in π conjugation of the aromatic ring and thus are less efficient H-bond acceptors.[49] The Ox^+ radical cation has been characterized by photoelectron spectroscopy,[54,55] and an accurate adiabatic ionization energy and several vibrational frequencies of the planar cation ground state are available from a high-resolution mass-analyzed threshold ionization spectrum. Photoelectron imaging of the oxazolide anion demonstrates selective deprotonation from the C2 position of the hetrocyclic ring.[56]

Information about H^+Ox and its clusters is scarce. Computations suggest exclusive N-protonation of the aromatic ring,[57,58] and the the recommended value for the proton affinity is tabulated as PA=876.4 kJ/mol.[59] Recently, we reported IR spectra of H^+Ox-L_n clusters with L=Ar (n≤2) and N_2 (n≤4) obtained by IR photodissociation (IRPD) of mass-selected clusters generated in a molecular plasma expansion.[60] Analysis of these spectra by dispersion-corrected density functional theory calculations at the B3LYP-D3/aug-cc-

pVTZ level provided the first spectroscopic proof that protonation of Ox indeed occurs exclusively at the N atom. In addition, the results yielded a first impression of the solvation process of H^+Ox with aprotic hydrophibic ligands, which occurs by the formation of linear and bifurcated NH…L and NH…L_2 bonds followed by further interior ion solvation.[60] Herein, we employ the same combined spectroscopic and computational approach to extend these studies on H^+Ox-L_n clusters to dipolar ligands, namely L=W=H_2O and n≤4, to characterize the differences of solvation of H^+Ox in a protic hydrophilic environment, which is relevant for understanding hydration effects of the protonated Ox building block in pharmaceutical applications.

2. Experimental Section

IRPD spectra of mass-selected H^+Ox-$W_{n\leq4}$ and tagged H^+Ox-$W_{n\leq2}$-N_2 clusters are recorded in the XH stretch range (X=C, N, O) in a tandem quadrupole mass spectrometer coupled to an electron ionization (EI) source and an octupole ion guide.[61,62] Briefly, H^+Ox-W_n(-N_2) clusters are produced in an ion source, which combines a pulsed supersonic expansion with electron and chemical ionization close to nozzle orifice. The expanding gas mixture is generated by seeding Ox (C_3H_3NO, Sigma-Aldrich, 98%, heated to 328 K) and H_2O (at room temperature) in carrier gas composed of N_2 and 5% H_2 in He in a 2:1 ratio at a backing pressure of 10 bar. Ox is protonated by exothermic proton transfer from H_3^+ and/or $H^+(H_2O)_n$ clusters produced by chemical ionization, and clusters of H^+Ox are then produced in the high-pressure regime of the supersonic expansion by three-body collisions. The desired parent clusters are mass-selected in the first quadrupole and irradiated in an adjacent octupole ion guide with a tunable IR laser pulse (ν_{IR}, 10 Hz, 2-5 mJ, bandwidth ~1 cm^{-1}) emitted from an optical parametric oscillator pumped by a Q-switched nanosecond Nd:YAG laser. Calibration of ν_{IR} to better than 1 cm^{-1} is achieved by a wavemeter. Resonant vibrational excitation followed by intracluster vibrational energy redistribution leads to the evaporation of the most weakly bound neutral ligand, according to:

$$H^+Ox\text{-}W_n + \nu_{IR} \rightarrow H^+Ox\text{-}W_{n-1} + W \quad (1)$$

$$H^+Ox\text{-}W_n\text{-}N_2 + \nu_{IR} \rightarrow H^+Ox\text{-}W_n + N_2 \quad (2)$$

Subsequently, the fragment ions are mass-selected by the second quadrupole and monitored with a Daly ion detector as a function of ν_{IR} to derive the IRPD spectrum of H^+Ox-W_n(-N_2). All IRPD spectra are linearly normalized for variations in the IR laser intensity measured with a pyroelectric detector. The contribution of metastable decay is subtracted from laser-induced dissociation by triggering the ion source at twice the laser repetition rate. The observed widths of the vibrational bands mainly arise from unresolved rotational structure, sequence hot bands involving inter- and intramolecular modes, and contributions from various structural isomers. Tagging with N_2 produces colder clusters because their maximum internal energy is given by the binding energy of the weakliest bonded ligand. As a consequence of the lower effective temperature, the spectra of the N_2-tagged clusters display higher spectral resolution.

3. Computational Details

Possible H^+Ox-W_n(-N_2) isomers are optimized at the B3LYP-D3/aug-cc-pVTZ level of theory to analyze the IRPD spectra.[63] This dispersion-corrected density functional reliably describes the electrostatic, induction, and dispersion forces of the investigated clusters.[64–69] Neutral Ox and Ox-W are also computed to derive the

impact of protonation on hydration on structure and intermolecular bonding. For energy optimization, the tight convergence criterion with ultrafine integration grid is used. In particular, the binding energy computed for the W_2 dimer (D_0=1103 cm^{-1}) is in excellent agreement with the measured value (D_0=1105±10 cm^{-1}),[70] indicating that the H-bond interactions in the hydration networks are modeled accurately by this computational approach. Fully relaxed potential energy surface calculations are performed during the search for stationary points, and their nature as minima or transition states is verified by harmonic frequency analysis. Harmonic intramolecular vibrational frequencies are subjected to a linear scaling factor of 0.9636, derived from a comparison of computed CH and OH stretch frequencies of neutral Ox and W, respectively, to their measured values.[46,71] For convenient comparison to the experiment, harmonic linear IR absorption stick spectra are convoluted with a Gaussian line shape (FWHM=10 cm^{-1}). All relative energies (E_e) and equilibrium dissociation energies (D_e) are corrected for harmonic zero-point vibrational energy to derive respective E_0 and D_0 values. Gibbs free energies are evaluated at 298 K (G_0). The total intermolecular dissociation energies are determined with respect to the molecular H^+Ox and W monomer fragments (also for the proton-transferred isomers of Ox-H^+W_4). The D_0 values reported for the tagged clusters correspond to binding energies of the N_2 ligand. Previous experience with the employed computational level demonstrates that basis set superposition errors are smaller than 1%,[67,68] and thus they are not considered further here. The atomic charge distribution and second-order perturbation energies ($E^{(2)}$) of the donor-acceptor orbital interaction involved in the H-bonds are evaluated using the natural bond orbital (NBO) analysis.[72,73] Further characterization of the H-bonds is achieved in noncovalent interaction (NCI) calculations by computing the reduced gradient of the electron density ρ, $s(\rho)\sim|\mathrm{grad}(\rho)|/\rho^{4/3}$, as a function of ρ oriented by the sign of second eigenvalue λ_2 of the Hessian, $\rho^*=\rho\,\mathrm{sign}(\lambda_2)$.[74,75] The relative strengths of various H-bonds can be estimated by comparing their respective ρ^* values.

4. Results & Discussion

All IRPD spectra of H^+Ox-W_n(-N_2) recorded between 2650 and 3820 cm^{-1} are compared in Figure 1. The positions and suggested vibrational and isomer assignments are listed in Table 1. The investigated spectral range covers the OH, NH, and CH stretch fundamentals ($\nu_{OH/NH/CH}$), which are sensitive to both the protonation site and the H-bonded hydration network. Significantly, the appearance of the H^+Ox-W_n spectra changes drastically as a function of cluster size, thus providing detailed information about the evolution of the cluster growth. In addition, the IRPD spectra of the colder N_2-tagged clusters display much narrower bands, which further facilitates the identification of the isomers observed for microhydrated H^+Ox. The bands A-C occur in the range of the free OH stretch modes of the W ligands (3600-3750 cm^{-1}). Transitions D occur only for the n≥2 cluster and vary strongly with the cluster size (3000-3400 cm^{-1}). Both their frequencies and band shapes suggest an assignment to bound OH stretch modes of the W ligands. Transition E at 3177±3 cm^{-1} is insensitive to n and has been assigned to CH stretch modes in the IRPD spectra of H^+Ox-L_n with L=Ar and N_2, where this band occurs at a very similar position (3168-3179 cm^{-1}).[60] The intense transitions F occur below 3000 cm^{-1}, as expected for bound NH stretch modes of cationic NH…O H-bonds. In the following, we discuss the evolution of the observed IRPD spectra as a function of cluster size with the aid of the DFT calculations and derive more precise vibrational and isomer assignments.

4.1 Ox, H^+Ox, and W

The geometric and vibrational properties of neutral Ox and H^+Ox calculated at the B3LYP-D3/aug-cc-pVTZ level are discussed in detail in our previous report.[60] The structure and vibrations computed for Ox agree satisfactorily with available experimental data.[46,52] The same is true for the corresponding predicted and measured properties of bare W (r_{OH}=0.9617 vs. 0.9578 Å, $\nu_{1/3}$=3656/3755 vs. 3657/3756 cm^{-1}).[71,76] Protonation of Ox at the N atom is energetically strongly favored over protonation at the O and C atoms of the heterocyclic ring (by more than 120 kJ/mol), and indeed our previous analysis of the IRPD spectra of H^+Ox-L_n with L=Ar and N_2 confirms exclusive N-protonation under the present experimental conditions. In addition, the experimental proton affinity recommended for Ox (PA=876.4 kJ/mol)[59] is in excellent agreement with our value computed for the N-protomer (876.7 kJ/mol).[60] Hence, we only consider this protomer further in the present study on H^+Ox-W_n. From the IRPD spectra of the π-bound H^+Ox-Ar/N_2 dimers, the free NH stretch frequency of bare H^+Ox is estimated as ν_{NH}=3444±3 cm^{-1},[60] in excellent agreement with the predicted value (3446 cm^{-1}). In conclusion, the employed theoretical level describes the relevant properties of the considered monomers to high accuracy.

4.2 H^+Ox-W and H^+Ox-W-N_2

In analogy to the H^+Ox-Ar/N_2 dimers,[60] we consider particularly the H-bound and π-bound H^+Ox-W structures (Figure 2). Because the intermolecular attraction in H^+Ox-W is dominated by electrostatic charge-dipole forces, all minima on the potential energy surface have the typical cation-dipole configuration with the O atom of W pointing toward the positive charge of H^+Ox. The global H-bonded H^+Ox-W(H) minimum, with a nearly linear NH…O ionic H-bond ($R_{NH...O}$=1.659 Å) and the plane of W perpendicular to the plane of H^+Ox, is nearly twice more stable than H^+Ox-W(π), D_0=6094 vs. 3334 cm^{-1}. This ionic H-bond is substantially stronger than the OH…N H-bond of the neutral Ox-W dimer (D_0=1697 cm^{-1}, $R_{OH...N}$=1.951 Å), in which W is H-bonded as proton donor to the in-plane lone pair of N in Ox (Figure S1 in the supporting information).[49,60] The strong H-bond in H^+Ox-W(H) significantly perturbs the NH group, resulting in a massive red shift and pronounced enhancement in the IR oscillator strength of the bound NH stretch mode (ν_{NH}^b) when compared to bare H^+Ox (Δr_{NH}=32.7 mÅ, $\Delta\nu_{NH}^b$=-546 cm^{-1}, ΔI_{NH}=1638 km/mol). The substantial PA of W (691 kJ/mol) facilitates H-bonding through a significant charge transfer from H^+Ox to W (Δq=0.06 e, Figure S2 in the supporting information),[59] which leads to slight red shifts and concomitant enhancement of IR intensities of the $\nu_{1/3}$ modes compared to bare W ($\Delta\nu_{1/3}$=-16/-29 cm^{-1}, $\Delta I_{1/3}$=51/88 km/mol). The barrier for internal rotation of W of V_b=281 cm^{-1} in H^+Ox-W(H) at the planar transition state is substantial (Figure S3 in the supporting information). As expected, the π-bound W ligand in H^+Ox-W(π) has no significant influence on the NH group, and the associated parameters are comparable to those of bare H^+Ox (Δr_{NH}=-1.8 mÅ, $\Delta\nu_{NH}$=19 cm^{-1}, ΔI_{NH}=-19 km/mol). Similar to H^+Ox-W(π), the H^+Ox-W(C5) structure with a CH…O ionic H-bond is a high-energy local minimum (D_0=3239 cm^{-1}), because the CH bonds are much less acidic than the NH group (Figure S4 in the supporting information). Attempts to optimize other structures with a CH…O H-bond failed (C2 and C4), probably because of very low barriers for W migration toward the nearby acidic NH group. Again, for the CH-bonded isomer, the perturbation of the NH group is minor.

To elucidate the effects of N_2 tagging on the H^+Ox-W dimer, we merely consider the by far most stable H^+Ox-W(H) isomer (Figure 2), because it is the only one observed experimentally (vide infra). The N_2 ligand is either H-bonded to W (D_0=937 cm^{-1}) or forms a π-bond with a smaller binding affinity (D_0=766 cm^{-1}). Although binding of N_2 to the CH groups is comparable in strength to π-bonding, this binding motif is not observed experimentally in the IRPD spectra of H^+Ox-$(N_2)_n$.[60] The cooperativity arising from the additional H-bonded N_2 ligand in H^+Ox-W(H)-N_2(H) increases the N-H bond length, leading to further lowering of ν_{NH}^b compared to H^+Ox-W(H), with Δr_{NH}=6.1 mÅ and ν_{NH}^b=2785 vs. 2883 cm^{-1}. In addition, the OH…N_2 H-bond elongates the O-H donor bond with a concomitant red shift of the coupled $\nu_{1/3}$ modes ($\Delta\nu_{1/3}$=-66/-22 cm^{-1}). On the contrary, the π-bound N_2 ligand in H^+Ox-W(H)-N_2(π) hardly affects the NH and OH groups. The slight increase in ν_{NH}^b (+26 cm^{-1}) is rationalized by noncooperative effects of interior ion solvation resulting from N_2 attachment at the π-site, which however barely influences the free $\nu_{1/3}$ modes (+1/+1 cm^{-1}).

The IRPD spectra of H^+Ox-W and H^+Ox-W-N_2 are compared in Figure 3 to the relevant computed spectra. The IRPD spectrum of H^+Ox-W exhibits an intense broad feature between 2650 and 3220 cm^{-1} (F1-F3, E) along with two relatively weak and narrower transitions at 3720 (A) and 3625 (B) cm^{-1}. Significantly, this spectrum lacks any signal of a ν_{NH}^f mode of H^+Ox near 3450 cm^{-1}. This observation implies that the NH group in H^+Ox-W is engaged in H-bonding to W, which immediately excludes any π-bonded or CH-bonded isomers (Figure 3, Figure S4 in the supporting information), consistent with the thermochemical predictions. The two bands B and A are then readily assigned to the free $\nu_{1/3}$ modes of the H^+Ox-W(H) global minimum computed as 3642/3728 cm^{-1}. The experimental red shifts of $\Delta\nu_{1/3}$=-31/-36 cm^{-1} are typical for cation-W bonding and consistent with the predictions (-16/-29 cm^{-1}). Clearly, the dissociation energy computed for this isomer (D_0=6094 cm^{-1}) is substantially larger than the absorbed photon energy (ν_{IR}), indicating that only internally hot clusters with E_{int}>3500 cm^{-1} are detected under the employed single-photon absorption conditions. This view is consistent with the large widths of the observed bands. The broad feature comprising bands F1-F3 and other unresolved peaks in the 2700-3200 cm^{-1} range are attributed to the ν_{NH}^b mode (predicted at 2883 cm^{-1}), which interacts with other combination bands and overtones (e.g., the overtone of the NH bend ($2\beta_{NH}$) predicted at 2932 cm^{-1}) via strong anharmonic coupling. Such a spectral feature is very typical for strong cationic NH…O H-bonds with W as proton acceptor, and has been observed for a variety of monohydrated aromatic clusters.[69,77,78] The transition with highest intensity (F3) probably carries the largest NH stretch character. Transition E at 3179 cm^{-1} is mostly assigned to two close-lying aromatic ν_{CH} modes, which are detected at ~3175 cm^{-1} for H^+Ox-Ar/N_2.[60] The relatively weak band X around 3230 cm^{-1} is tentatively assigned to the OH bending overtone of W predicted near 3226 cm^{-1} from the harmonic analysis (using 0.98 as scaling factor).

The assignment of the H^+Ox-W spectrum to the hot population of the single H^+Ox-W(H) isomer is supported by the IRPD spectrum of cold H^+Ox-W-N_2 clusters in Figure 3. Tagging with N_2 drastically reduces the maximum internal energy to below 1000 cm^{-1} and facilitates single-photon IRPD from the ground vibrational state of the clusters. As a result, the widths of the transitions are narrower and the appearance of the spectrum in the ν_{NH}^b range is cleaner. The OH stretch bands B and A of the tagged cluster at 3610 and 3711 cm^{-1} are red shifted from those of the bare dimer ($\Delta\nu_{1/3}$=-15/-9 cm^{-1}), suggesting that the N_2 ligand forms a H-bond to the W ligand, H^+Ox-W(H)-N_2(H), so that we can exclude isomers with CH-bonded or π-

bonded N_2 ligands. The harmonic calculations overestimate these shifts ($\Delta\nu_{1/3}$=-66/-22 cm^{-1}), partly because of the high temperature of the untagged monohydrate. The width of the intense H-bonded transition F is remarkably reduced upon cooling with the N_2 tag, and the extracted ν_{NH}^{b} fundamental of 2970 cm^{-1} is to be compared to the computed value of 2785 cm^{-1}. This discrepancy may be attributed to the highly anharmonic nature of this H-bonded oscillator. Furthermore, the measured intensity ratio of the ν_{CH} band (E at 3178 cm^{-1}) relative to the ν_{NH}^{b} band in the tagged spectrum agrees well with the predictions, confirming that anharmonic couplings and effects of hot bands are drastically reduced for the cold N_2-tagged ions. This spectral behavior upon tagging is again typical for strong cationic NH…O H-bonds of aromatic cations with W.[69,77,78]

4.3 H^+Ox-W_2 and H^+Ox-W_2-N_2

In the most stable H^+Ox-W_2(H) structure, a H-bonded W_2 dimer forms an NH…O H-bond to H^+Ox with a total interaction energy of D_0=10278 cm^{-1} (Figure 4). The formation of such a H-bonded network is strongly cooperative in nature. For example, D_0 of H^+Ox-W_2 is 43% larger than the sum of the binding energies of W_2 and H^+Ox-W (D_0=1103+6094=7197 cm^{-1}). Similarly, the intermolecular NH…O and OH…O H-bonds of the two units contract drastically ($R_{NH...O}$=1.555 vs. 1.659 Å, $R_{OH...O}$=1.712 vs. 1.947 Å). This large cooperatively can mostly be traced back to the substantially increased PA of W_2 as compared to W (PA=808 vs. 691 kJ/mol)[59,79] and the strong polarization effects induced by the positive charge of the excess proton. As a result, the N-H bond gets further elongated upon attachment of the second W (Δr_{NH}=21 mÅ) and the total red shift and IR oscillator strength of the ν_{NH}^{b} mode become more pronounced ($\Delta\nu_{NH}$=-892 vs. -563 cm^{-1}, I_{NH}=2853 vs. 1840 km/mol). The increased distance of the terminal W from the positive charge results in a slight blue shift in $\nu_{1/3}$ compared to the dimer ($\Delta\nu_{1/3}$=+9/+11 cm^{-1}). The new free OH stretch mode (ν_f) of the first W ligand is predicted between the two $\nu_{1/3}$ modes at 3712 cm^{-1}, whereas its H-bonded OH stretch mode (ν_{OH}^{b}) is strongly red shifted down to 3267 cm^{-1}, consistent with its longer bond length (Δr_{OH}=23.5 mÅ). This red shift is much larger than for bare W_2 (ν_{OH}^{b}=3601 cm^{-1})[80–82] because of the strong cooperativity effect on the W-W H-bond introduced by the presence of the H^+Ox cation. Other isomers of H^+Ox-W_2 with two individual W ligands attached to H^+Ox are less favorable, because binding sites other than the NH group (e.g., π or CH) are less favorable and interior ion solvation is noncooperative in nature. This is illustrated for the example of the H^+Ox-W_2(I) isomer shown in Figure 4, in which two W ligands are separately H-bonded to the NH and C5H groups (D_0=8955 cm^{-1}). The noncooperativity in binding energy amounts to 8955/(3239+6094)=0.96 or 4% for this isomer. Apart from this thermochemical argument, the IRPD spectrum of H^+Ox-W_2 in Figure 1 shows a drastic change in the ν_{NH}^{b} range compared to that of H^+Ox-W, indicating that the second W ligand is strongly perturbing the NH group, which can only be for the H^+Ox-W_2(H) structure with a H-bonded W_2 unit.

We consider the three main binding motifs for attachment of N_2 to H^+Ox-W_2(H) shown in Figure 4, namely H-bonding to a free OH group of the W_2 unit and π-bonding to H^+Ox. N_2-bonding to CH groups is energetically less favorable and indeed not observed for H^+Ox-$(N_2)_n$.[60] In the most stable H^+Ox-W_2(H)-N_2(H1) isomer (D_0=789 cm^{-1}), N_2 forms a H-bond to the remaining free OH group of the first W ligand, resulting in a slight elongation of the O-H bond with a concomitant decrease in ν_f (Δr_{OH}=3 mÅ, $\Delta\nu_{OH}$=-69 cm^{-1}). In the less stable H^+Ox-W_2(H)-N_2(H2) isomer, the N_2 ligand binds to the terminal W ligand. It is thus further away from

the positive charge leading to a lower binding energy (D_0=694 cm^{-1}) and longer OH…N_2 bond. As a result, the red shifts of $\nu_{1/3}$ from free W are smaller ($\Delta\nu_{1/3}$=-39/-19 cm^{-1}) than for the analogous H^+Ox-W(H)-N_2(H) structure. In both isomers H^+Ox-W_2(H)-N_2(H1/2), the additional H-bonded N_2 ligand slightly strengthens (and contracts) the NH…O H-bond between H^+Ox and W_2, because of the cooperativity of the H-bonded network and the higher PA of W_2-N_2 compared to W_2. This in turn is visible in a modest elongation of the N-H bond and a small red shift in ν_{NH}^{b}. In contrast, the additional π-bound N_2 ligand in H^+Ox-W_2(H)-N_2(π) is mostly stabilized by charge-quadrupole and charge-induced dipole interactions, resulting in a D_0 value (695 cm^{-1}) similar to that of H^+Ox-W_2(H)-N_2(H2). As expected, π-tagging has no significant effect on the IR spectrum of H^+Ox-W_2(H) in the XH stretch range.

The IRPD spectra recorded for H^+Ox-W_2 and H^+Ox-W_2-N_2 are compared in Figure 5 to the relevant computed spectra. The spectrum of bare H^+Ox-W_2 is drastically different from that of the *n*=1 cluster (Figure 1). For example, it no longer exhibits the broad transitions F1-F3. Instead, we observe a rising signal toward the red end of the scan (2650 cm^{-1}), which we tentatively assign to the blue tail of ν_{NH}^{b}, yielding an upper limit of the ν_{NH}^{b} fundamental predicted at 2554 cm^{-1}. This drastic spectral change in the ν_{NH}^{b} range confirms that the second W ligand binds to the first one. The new feature C at 3705 cm^{-1} lies between the transitions B (3649 cm^{-1}) and A (3745 cm^{-1}) and agrees well with the predicted ν_f mode (3712 cm^{-1}) of the first W ligand next to the positively charged H^+Ox. The other two transitions B and A in the free OH stretch range are readily assigned to $\nu_{1/3}$ of the terminal W ligand predicted at 3651 and 3739 cm^{-1}, which are indeed blue-shifted from the corresponding transitions of H^+Ox-W, because of the larger separation of the terminal W from the center of the positive charge. The other new and rather intense feature D at 3338 cm^{-1} is safely attributed to the H-bonded OH stretch mode of the W_2 unit in H^+Ox-W_2(H) predicted at ν_{OH}^{b}=3267 cm^{-1}. Again, the predicted harmonic frequency shift somewhat overestimates the measured shift of the fundamental frequency upon H-bonding, due to the strongly anharmonic nature of the proton-donor stretch mode. As predicted, the H-bonded OH stretch frequency in H^+Ox-W_2 is much lower than in isolated W_2 (3338 vs. 3601 cm^{-1}) due to the large cooperativity.[80,81] Band E at 3179 cm^{-1} in the H^+Ox-W_2 spectrum is unshifted from the *n*=1 spectrum, which confirms its assignment to the aromatic ν_{CH} modes. Closer inspection reveals some signal between bands E and D above the background (band X, 3247 cm^{-1}), which we tentatively assign to the bending overtones of the W ligands, $2\beta_{OH}$, predicted at 3261 and 3209 cm^{-1}. In conclusion, all major features of the H^+Ox-W_2 spectrum can reliably be attributed to the most stable isomer, which features a H-bonded solvent network. This result is qualitatively different from the H^+Ox-L_n structures with L=Ar and N_2, in which the aprotic ligands bind individually to the central H^+Ox cation at various binding sites (interior ion solvation).

Similar to the *n*=1 case, the IRPD spectrum of tagged H^+Ox-W_2-N_2 in Figure 5 features bands with narrower widths due to the reduced internal energy. In general, it confirms the spectral features and assignments of the bare cluster. The most striking difference is the relative intensity of band C1 at 3707 cm^{-1} assigned to ν_f of the first W ligand, which is strongly reduced in intensity by N_2 tagging compared to bands B and A but keeps its position compared to the *n*=1 spectrum (3705 cm^{-1}). Such an effect is expected for the predominant presence of the most stable H^+Ox-W_2(H)-N_2(H1) isomer, in which this free OH group is solvated by N_2, which shifts this mode to the red. Following this scenario, bands D, C2, and A at 3312, 3667, and

3742 cm^{-1} are assigned to ν_{OH}^{b}, ν_f, and ν_3 modes of H^+Ox-W_2(H)-N_2(H1). Its N_2-bonded ν_f transition overlaps with band C2. The remaining weak band C1 must be ascribed to the ν_f mode of the much less abundant local minima, H^+Ox-W_2(H)-N_2(H2) and/or H^+Ox-W_2(H)-N_2(π). Like for the spectrum of the untagged cluster, the transitions E and X in the H^+Ox-W_2-N_2 spectrum are attributed to the ν_{CH} and $2\beta_{OH}$ vibrations. Careful analysis of the high-frequency range reveals that band C2 at 3667 cm^{-1} exhibits a shoulder at 3657 cm^{-1} (B), which is attributed to ν_1 of H^+Ox-W_2(H)-N_2(H1/π).

4.4 H^+Ox-W_3

We consider the two most stable H^+Ox-W_3 geometries that are obtained by adding a third W ligand to either the first or the second W ligand of H^+Ox-W_2(H). The branched H^+Ox-W_3(b) isomer with C_s symmetry is calculated to be slightly more stable than the chain-type H^+Ox-W_3(l) isomer with a linear H-bonded W_3 chain (D_0=13908 *vs.* 13582 cm^{-1}). The cooperativity is slightly stronger for the branched isomer (67.4 vs. 63.6%) because of hydration closer to the positive charge of H^+Ox. The additional W in H^+Ox-W_3(b) further strengthens the NH…O H-bond as compared to the *n*=2 case ($\Delta R_{NH...O}$=-101 mÅ), consistent with the larger PA of W_3 compared to W_2 (862 *vs.* 808 kJ/mol).[79,83] As a result, the N-H bond elongates from 1.066 to 1.099 Å, and the total red shift of ν_{NH}^{b} increases from -892 to -1339 cm^{-1}. The free $\nu_{1/3}$ modes of the terminal W ligands are calculated at 3654 and 3744 cm^{-1}, while the H-bonded antisymmetric and symmetric ν_{OH}^{b} frequencies of the first W are strongly reduced to 3384 and 3349 cm^{-1}, respectively.

The linear W_3 chain in the H^+Ox-W_3(l) isomer has a less pronounced effect on the NH group as compared to the branched isomer, with a weaker NH…O H-bond ($R_{NH...O}$=1.507 vs. 1.454 Å) and thus a smaller N-H bond elongation and less pronounced total ν_{NH}^{b} red shift (r_{NH} = 1.0799 Å, $\Delta\nu_{NH}^{b}$=-1092). Its $\nu_{1/3}$ modes of the terminal W are comparable to those of the branched isomer. However, the linear W_3 network features characteristics free ν_f modes of the two dangling OH groups calculated at 3717 and 3715 cm^{-1}. The ν_{OH}^{b} mode of the first OH…O H-bond closer to the H^+Ox positive charge is much further red shifted compared to the remaining ν_b oscillator of the second OH…H H-bond (3046 vs. 3374 cm^{-1}).

The IRPD spectrum of H^+Ox-W_3 is compared in Figure 7 to the IR spectra computed for the two considered isomers. The IRPD spectrum exhibits four major bands at 3743 (A), 3654 (B), 3348 (D1), and 3178 (E) cm^{-1}. Transition D1 has a blue-shaded contour, which is characteristic of a proton-donor stretch band. These four bands are readily assigned to the transitions of the most stable H^+Ox-W_3(b) isomer predicted at 3744 (ν_3), 3654 (ν_1), 3384 (antisymmetric ν_{OH}^{b}), 3349 (symmetric ν_{OH}^{b}), and 3160 (most intense ν_{CH}), respectively. Additionally, the weak feature X at 3242 cm^{-1} is tentatively assigned to $2\beta_{OH}$ of the water ligands. The good agreement between experimental and computed IR spectra demonstrates that the branched isomer dominates the H^+Ox-W_3 population, consistent with its higher D_0 value. In addition to the major peaks, the IRPD spectrum exhibits two weaker and less resolved bands at 3707 (C) and 3050 (D2) cm^{-1}, which indicate a very weak population of the less stable H^+Ox-W_3(l) isomer. The intensity of band C, which is assigned to the two overlapping and nearly degenerate ν_f modes of H^+Ox-W_3(l) predicted at 3717 and 3715 cm^{-1}, is dramatically reduced as compared to H^+Ox-W_2, confirming the predominant population of the branched

isomer. The remaining weak feature D2 is attributed to the ν_{OH}^{b} mode predicted at 3046 cm^{-1} with high intensity (1548 km/mol).

4.5 $H^+Ox\text{-}W_4$

The potential energy surface becomes substantially more complex for increasing degree of hydration. Thus, the search for low-energy minima of $H^+Ox\text{-}W_4$ is less complete. To this end, we consider the four low-energy $H^+Ox\text{-}W_4$ structures shown in Figure 6. The branched and linear $H^+Ox\text{-}W_4$(b/l) isomers feature a NH…O type H-bond of H^+Ox to the H-bonded W_4 network and are obtained by simply adding a fourth W ligand in the outermost shell of the two corresponding n=3 isomers. As for the n=3 case, the branched structure is more stable than the linear structure for n=4, because the W ligands are closer to the excess proton (D_0=17067 vs. 16425 cm^{-1}). For these structures, the cooperativity in binding energy amounts to 7764 and 7022 cm^{-1} (81.5 and 74.7%). In the other two cyclic $H^+Ox\text{-}W_4$(c1/c2) isomers, the first three W molecules form a H-bonded solvent ring involving the NH and adjacent CH groups of H^+Ox (C2H or C4H) as proton donors in NH…O and CH…O type H-bonds. The remaining fourth W ligand is then H-bonded with one of the peripheral W ligands in the second hydration shell. Thus, the cyclic isomers have one more H-bond than the branched and linear isomers. As a result of the additional CH…O H-bond, the $H^+Ox\text{-}W_4$(c1) isomer has the highest stability (D_0=17169 cm^{-1}) of all isomers considered. $H^+Ox\text{-}W_4$(c2) has a somewhat lower binding energy (D_0=16495 cm^{-1}), partly because the C4H group is less acidic than the C2H group,[60] leading to a slightly weaker and longer CH…O H-bond ($R_{CH...O}$=2.077 vs 2.062 Å). On the other hand, the strong NH…O ionic H-bond in the cyclic isomers is somewhat weaker than in the branched and linear isomers ($R_{NH...O}$=1.539 and 1.542 Å *vs.* 1.389 and 1.454 Å), because of the additional constraints on the H-bonded solvent network imposed by the additional CH…O H-bond. In fact, no cyclic stable structure is found for the cluster size n=3. Similarly, no cyclic n=4 structure with all four W ligands participating in the water ring is obtained. Except for $H^+Ox\text{-}W_4$(l), all structures feature a three-coordinated W ligand. However, its nature in terms of number of donor and acceptor H-bonds is different for different isomers (double-donor single-acceptor or single-donor double-acceptor). The ν_{OH}^{b} frequencies of the W_4 network within these structures span a wide range and depend sensitively on the respective solvation environment. In comparison to the free ν_{CH} modes of the linear and branched isomers, the IR intensity of the H-bonded ν_{CH}^{b} mode of the cyclic structures is significantly enhanced with a concomitant red shift of its frequency (ν_{CH}^{b}=3027 and 3104 cm^{-1} for the cyclic isomers, 3155<ν_{CH}<3190 cm^{-1} for the noncyclic structures).

The proton affinity of W_n clusters increases with cluster size n (PA=691, 808, 862, and 900 kJ/mol for n=1-4)[59,79,83] and exceeds the value for N-protonated H^+Ox (PA=876 kJ/mol) for clusters larger than n≥4 by more than 20 kJ/mol (or 1700 cm^{-1}). Hence, from these values alone, one may expect intracluster proton transfer from H^+Ox to W_n in $H^+Ox\text{-}W_n$ clusters to occur for n>3, leading to the formation of $Ox\text{-}H^+W_n$ clusters. However, in addition to the PA values one must also consider the difference in the intermolecular solvation energies, which may partly compensate for the PA difference.[84-87] In addition, the W_n structures in $H^+Ox\text{-}W_n$ and the H^+W_n structures in $Ox\text{-}H^+W_n$ differ from those of bare W_n and H^+W_n, so that the effective PA values are modified accordingly. For this reason, the four $H^+Ox\text{-}W_4$ isomers shown in Figure 6 are actually quite stable non-proton-transferred isomers, although the PA values of bare W_4 and Ox alone clearly suggest exothermic intracluster proton transfer. The most stable proton-transferred $Ox\text{-}H^+W_4$(1/2) structures shown in

Figure 6 have indeed binding energies (D_0=17054 and 16109 cm^{-1}) comparable to those of the $H^+Ox\text{-}W_4$ isomers but do not reach the stabilization of the $H^+Ox\text{-}W_4$(c1) isomer, which remains the global minimum. These two $Ox\text{-}H^+W_4$(1/2) structures differ in the position of the neutral Ox ligand in the hydration shell of H^+W_4. While in $Ox\text{-}H^+W_4$(1) the Ox ligand is a member of the Eigen-type ion core with direct contact to the central H_3O^+ ion, it binds in $Ox\text{-}H^+W_4$(2) in the first solvation shell to a distorted $H_9O_4^+$ core, thus leading to a smaller total binding energy. From the bare consideration of the computed dipole moments of Ox and W (1.54 and 1.85 D) and the resulting charge-dipole interaction, one would actually expect $Ox\text{-}H^+W_4$(2) to be more stable than $Ox\text{-}H^+W_4$(1). Apparently, the larger cooperativity of the H-bonded network in $Ox\text{-}H^+W_4$(1) overrides this difference in electrostatic attraction and brings the Ox ring into the first solvation shell of H_3O^+. As a result, the OH…N ionic H-bond in $Ox\text{-}H^+W_4$(1) is much stronger than in $Ox\text{-}H^+W_4$(2), $R_{OH...N}$=1.438 vs. 1.621 Å. Interestingly, the $Ox\text{-}H^+W_4$(1) and $H^+Ox\text{-}W_4$(b) isomers are structurally very similar except for the position of the proton. Both nearly isoenergetic minima (ΔE_0=115 cm^{-1}) are separated by only small barriers of less than 200 cm^{-1} for proton transfer along the N…H^+…O coordinate, suggesting that the zero-point energy level lies above the transition state for this slightly asymmetric double-minimum potential (Figure S5 in the supporting information), leading to a single species with a largely delocalized shared proton.

Unlike the smaller $H^+Ox\text{-}W_{n\leq3}$ clusters, the IRPD spectrum is more congested for n=4 (Figure 1 and 8). The broad feature below 3500 cm^{-1} shows few unresolved and strongly overlapping bands, which are compatible with the simulated spectra of all considered isomers. The transitions E and X at 3180 and 3247 cm^{-1}, respectively, are consistent with the band positions of the n≤3 clusters. Consequently, these two features are assigned to the ν_{CH} and $2\beta_{OH}$ vibrations, respectively. However, this spectral range also exhibits contributions from the ν_{OH}^{b} modes of both $H^+Ox\text{-}W_4$ and $Ox\text{-}H^+W_4$ type structures. The new and relatively weak feature at 3567 cm^{-1} (Y) can be explained only by the ν_{OH}^{b} mode of the W ligand involved in the CH…W H-bond of the cyclic $H^+Ox\text{-}W_4$(c2) isomer. Similarly, the weakly resolved transition H (3084 cm^{-1}), which is absent in the smaller n=2-3 clusters, is attributed to the H-bonded red-shifted ν_{CH}^{b} modes of the two considered cyclic structures. These observations may be taken as experimental evidence for the competitive stability of cyclic $H^+Ox\text{-}W_4$ isomers predicted by the DFT calculations. Similar to the n=2-3 clusters, the transitions at 3651 (B), 3715 (C), and 3741 (A) cm^{-1} are attributed to ν_1, ν_f, and ν_3 modes, which are characteristic of all calculated structures. Interestingly, the experimental intensity of band C increases compared to n=3. In general, it is difficult to exclude any of the calculated structures, and other isomers not considered in the calculations may also contribute. Despite the higher PA of W_4 in comparison to Ox, no unequivocal signature of the intracluster proton transfer is detected. However, proton-transferred structures are energetically comparable to the non-proton-transferred structures. Thus, we assume the presence of both types of geometries in our the ion source.

4.6 Cluster Growth

The analysis of the IRPD spectra $H^+Ox\text{-}W_n$ with the aid of DFT calculations provides a clear picture of the cluster growth and the initial microhydration steps of H^+Ox. Clearly, the formation of a H-bonded W_n solvent network attached to the acidic NH group of N-protonated H^+Ox is energetically strongly favoured over interior ion solvation because of the large cooperative effects of ionic H-bonding. The most stable computed H^+Ox-

W_n clusters H^+Ox-W(H), H^+Ox-W_2(H), H^+Ox-W_3(b), and H^+Ox-W_4(c1) for n=1-4 are consistent with the experimental IRPD spectra, and the population of the n=1-3 clusters are strongly dominated by a single isomer corresponding to the global minimum. For n=4, several low-energy isomers compet,. In particular, cyclic structures with a weak second H-bond contact (CH…O) are observed as new low-energy isomers. Because the proton affinity of W_n clusters increases with cluster size (PA=691, 808, 862, 900 kJ/mol for n=1-4), its NH…O ionic H-bond to the acidic NH group of N-protonated H^+Ox becomes stronger and shorter ($R_{NH...O}$=1.659>1.555>1.454>1.389 Å for n=1-4; we consider here the H^+Ox-W_4(b) isomer, because its H-bond network is not perturbed by the CH…O H-bond), leading to a pronounced increasing red shift in ν_{NH}^{b} ($\Delta\nu_{NH}^{b}$=-563, -892, -1339, -1671 cm^{-1} for n=1-4, Figure 9). The red shift is so large that the ν_{NH}^{b} transition is here only observed for n=1, because the intensity of the employed IR-OPO laser is too low below 2600 cm^{-1} to drive IRPD of the strongly bonded W ligands. The total binding energy increases as D_0=6094 < 10278 < 13908 < 17067 cm^{-1} for n=1-4, yielding incremental hydration energies of 6094, 4184, 3630, and 3159 cm^{-1}, which are all substantially larger than the dissociation energy of the W_2 dimer (1108 cm^{-1}), illustrating the large polarization effect of the excess H^+ on the W_n network. The increasing strength of the ionic NH…O bond as a function of hydration is accompanied by increasing charge transfer to the solvent cluster (Δq=0.060, 0.091, 0.129, and 0.161 e for n=1-4, Figure S2 in the supporting information). This trend is in line with the $E^{(2)}$ energies and ρ^* values of the NH…O H-bond derived from NBO and NCI calculations ($E^{(2)}$=106.1, 161.5, 241.7, 318.5 kJ/mol; -ρ^*=0.0498, 0.0656, 0.0862, 0.1033 a.u. for n=1-4, Figures S6 and S7 in the supporting information). For clusters with n≥4, proton transfer for H^+Ox to the W_n cluster becomes energetically competitive according to the DFT calculations and the comparison of proton affinity values (Figure S8 in the supporting information). Experimentally, the IRPD spectrum of n=4 is not of sufficient resolution to decide this aspect. Clearly, although solvation energy is in favour of protonation of Ox, the most stable clusters with larger n will ultimately be of the type Ox-H^+W_n with a neutral Ox ligand being located on the surface, because the excess proton in H^+W can be stabilized more efficiently.

Tagging of the H^+Ox-W_{1-2} clusters with N_2 significantly reduces their internal energy, resulting in narrower transitions in IRPD spectra with higher resolution. The tagged water complexes prefer N_2 attachment through H-bond formation adjacent to the positive charge.

4.7 Comparison to Neutral Ox-W

To evaluate the effects of protonation of Ox on the microhydration structure, it is instructive to compare the properties of H^+Ox-W_n with those of the neutral Ox-W_n clusters. Unfortunately, no experimental information is available for any Ox-L_n cluster and computational studies are limited to the Ox-W dimer.[48] In the global minimum of Ox-W, W binds to the in-plane lone pair of the basic N atom of Ox via a linear OH…N H-bond (D_0=1697 cm^{-1}, $R_{OH...N}$=1.951 Å, Figure S1 in the supporting information), which is indeed much weaker than the ionic NH…O H-bond in the N-protonated H^+Ox-W(H) dimer (D_0=6094 cm^{-1}, $R_{NH...O}$=1.659 Å), indicating the drastic change of protonation on the interaction potential with respect to both the global minimum structure (orientation of the W ligand) and the interaction strength. Stable structures with other possible binding sites of W to neutral Ox (e.g., π and O) do not converge at the B3LYP-D3/aug-cc-pVTZ level employed herein. In particular, the local minimum obtained in Ref. 48 at the MP2 and B3LYP levels using the

smaller 6-31+G* basis set (with a C5H…O and OH…O H-bond) can not be reproduced herein at the higher computational level with the much larger basis set and proper inclusion of dispersion. Interestingly, the lower-level calculations predict for the Ox-W global minimum a much longer H-bond ($R_{OH...N}$ =2.010 Å), along with a much higher binding energy (D_0~2550 cm^{-1})[48] than our more reliable B3LYP-D3/aug-cc-pVTZ approach.

4.8 Comparison to $H^+Ox\text{-}L_n$ Clusters with Aprotic Ligands

The microhydration process of H^+Ox with protic, hydrophilic, and dipolar W molecules differs qualitatively from solvation with aprotic, hydrophobic, and nonpolar (L=Ar) or quadrupolar ($L=N_2$) ligands characterized previously by the same experimental and computational approach.[60] For the latter solvents, the L…L interaction is much weaker than the H^+Ox…L interaction (<100 cm^{-1})[62] and no strong H-bonded network can be formed. As a result, $H^+Ox\text{-}(Ar/N_2)_n$ clusters prefer interior ion solvation, in which individual ligands are attached to the H^+Ox cation core, first by H-bonding to the NH group, and subsequently by attachment to the less stable π and CH binding sites. In contrast, $H^+Ox\text{-}W_n$ clusters prefer the formation of the H-bonded solvent network, because of the strong cooperativity of H-bonding discussed above. Common to all H^+Ox-L dimers is that the global minimum on the potential is the H-bonded H^+Ox-L(H) structure with a linear NH…L ionic H-bond of the neutral ligand to the highly acidic proton of the NH group of H^+Ox. Again, the interaction strength is strongly correlated with the PA of L (PA=369<494<691 kJ/mol for Ar, N_2, and W),[59] D_0=891<1597<6094 cm^{-1},[60] as illustrated in Figure 9. As a result, the NH…L ionic H-bond to the acidic NH group of N-protonated H^+Ox becomes stronger and shorter ($R_{NH...L}$=2.420>2.031>1.659 Å), leading to an increasing predicted red shift in $\nu_{NH}{}^b$ ($\Delta\nu_{NH}{}^b$=-70, -157, -546 cm^{-1}), consistent with the observed values (-52, -126, -611 (considering F3) cm^{-1}). This trend in H-bond strength is also visible in the charge transfer from H^+Ox to L (Δq=0.017, 0.028, 0.060 e), the $E^{(2)}$ energies (13.7, 42.2, 106.1 kJ/mol) and the ρ^* values (-0.013, -0.022, -0.0498 a.u.).

5. Conclusions

In this work, we characterized microhydrated clusters of H^+Ox by IR photodissociation spectroscopy of size-selected $H^+Ox\text{-}W_n$ clusters and dispersion-corrected DFT calculations to determine for the first time the protonation site and the most stable structure of the solvation network of this prototypical protonated azole ring. Tagging of the hydrated cluster up to n=2 with N_2 results in internally colder clusters and thus spectra with higher resolution. Systematic shifts in the OH, NH, and CH stretch frequencies as a function of the cluster size provide a consistent picture of the sequential cluster growth. The salient results may be summarized as follows. Protonation of Ox in the H_2-containing plasma occurs at the most basic N atom of the heterocyclic ring. The spectra of the n=1-3 clusters are dominated by the most stable isomer predicted by the DFT calculations. Microhydration of H^+Ox occurs by solvating the acidic NH proton of H^+Ox with a H-bonded W_n cluster via a strong ionic NH…O H-bond. The formation of such H-bonded networks is strongly cooperative and the strength of the NH…O bond increases with n, because the proton affinity of W_n increases with size. At the cluster size n=4, structures with nearly barrierless proton transfer to the solvent, $Ox\text{-}H^+W_4$, are predicted to become energetically competitive with structures of the type $H^+Ox\text{-}W_4$, because the larger solvation energy can compensate for the difference in proton affinity of Ox and W_4 (~25 kJ/mol).

Indeed, in contrast to the *n*=1-3 spectra, the *n*=4 spectrum is significantly more congested indicating the presence of more than one isomer, including the likely formation of proton-transferred structures. We expect that in the most stable clusters with *n*≥5 a neutral Ox ring binds at the surface of a H^+W_n cluster, and this intracluster proton transfer is an important process toward understanding the physiological activity of Ox-bearing biomolecules in microhydrated environments. Comparison of H^+Ox-W_n with the previously studied H^+Ox-L_n clusters with L=Ar and N_2 reveals importan differences in the solvation of H^+Ox with hydrophilic and hydrophobic ligands. While the dipolar protic W ligands form a H-bonded solvent network attached to the NH proton of H^+Ox, the aprotic nonpolar and quadrupolar Ar and N_2 ligands prefer interior ion solvation by attachment of individual ligands around the heterocyclic aromatic cation. In all cases, the global minimum of the H^+Ox-L dimer features a linear NH…L ionic H-bond, and the strength of this H-bond increases in the order Ar<N_2<W, in line with the increasing proton affinity of the ligand. This trend is also visible in the red shift of the proton donor stretch vibration (ν_{NH}^{b}), as well as the computed binding energies and the NBO and NCI analyses. Finally, protonation of Ox has a strong impact on the interaction potential with W, with respect to both its structure and binding energy. While Ox-W has a weakly H-bonded structure with W acting as proton donor in an OH…N H-bond, H^+Ox-W features a strong ionic NH…O H-bond with W being a proton acceptor. Such charge-induced structural changes are typical for (mono-)hydrated aromatic molecules.[10,62,68,85-92]

Acknowledgements

This study was supported by Deutsche Forschungsgemeinschaft (DO 729/3-3).

Supporting Information

Additional optimized structures, energies, calculated IR spectra, NBO atomic charges, $E^{(2)}$ energies, and ρ^* values of selected H^+Ox-W_n isomers and Ox-W, along with proton affinities of W_n and Ox.

Figure Captions

Figure 1. Comparison of IRPD spectra of $H^+Ox\text{-}W_n$ (n=1-4) and $H^+Ox\text{-}W_n\text{-}N_2$ (n=1-2) clusters measured between 2650 and 3820 cm^{-1}. The positions of the transitions observed are listed in Table 1, along with the suggested vibrational and isomer assignments.

Figure 2. Optimized geometries of W, H^+Ox (N-protonated, with atomic numbering), and most stable isomers $H^+Ox\text{-}W$ and $H^+Ox\text{-}W\text{-}N_2$ calculated at the B3LYP-D3/aug-cc-pVTZ level. Binding energies (D_0) and bond lengths are given in cm^{-1} and Å, respectively. Numbers in parentheses correspond to relative energies and free energies in cm^{-1} (E_0, G_0).

Figure 3. Comparison of measured IRPD spectra of $H^+Ox\text{-}W$ and $H^+Ox\text{-}W\text{-}N_2$ to linear IR absorption spectra computed for the most stable isomers at the B3LYP-D3/aug-cc-pVTZ level. For comparison, the IR spectra calculated for bare H^+Ox and W are also shown. The IR stick spectra are convoluted with Gaussian line profiles with FWHM=10 cm^{-1}.

Figure 4. Optimized geometries of W_2, $H^+Ox\text{-}W_2$, and most stable isomers of $H^+Ox\text{-}W_2\text{-}N_2$ obtained at the B3LYP-D3/aug-cc-pVTZ level. Binding energies (D_0) and bond lengths are given in cm^{-1} and Å, respectively. Numbers in parentheses correspond to relative energies and free energies in cm^{-1} (E_0, G_0).

Figure 5. Comparison of measured IRPD spectra of $H^+Ox\text{-}W_2$ and $H^+Ox\text{-}W_2\text{-}N_2$ to the linear IR absorption spectra computed for the most stable isomers at the B3LYP-D3/aug-cc-pVTZ level. For comparison, the IR spectra calculated for bare W_2 is also shown. The IR stick spectra are convoluted with Gaussian line profiles with FWHM=10 cm^{-1}.

Figure 6. Optimized geometries of $H^+Ox\text{-}W_n$ and $Ox\text{-}H^+W_n$ clusters with n=3 and 4 obtained at the B3LYP-D3/aug-cc-pVTZ level. Binding energies (D_0) and bond lengths are given in cm^{-1} and Å, respectively. Numbers in parentheses correspond to relative energies and free energies in cm^{-1} (E_0, G_0).

Figure 7. Comparison of measured IRPD spectrum of $H^+Ox\text{-}W_3$ to the linear IR absorption spectra computed for the two most stable isomers at the B3LYP-D3/aug-cc-pVTZ level. The IR stick spectra are convoluted with Gaussian line profiles with FWHM=10 cm^{-1}.

Figure 8. Comparison of measured IRPD spectrum of $H^+Ox\text{-}W_4$ to the linear IR absorption spectra computed for the most stable isomers of $H^+Ox\text{-}W_4$ and $Ox\text{-}H^+W_4$ at the B3LYP-D3/aug-cc-pVTZ level. The IR stick spectra are convoluted with Gaussian line profiles with FWHM=10 cm^{-1}.

Figure 9. Observed (filled circles) and calculated (open circles, B3LYP-D3/aug-cc-pVTZ) $\nu_{NH}{}^b$ frequencies of the H-bonded $H^+Ox\text{-}L$ (L=Ar, N_2, W) dimers and $H^+Ox\text{-}W_n$ clusters as a the function of the PA of the ligands. For n=4, we consider both the c1 and b isomers. The c1 isomer is most stable but its NH…O H-bond is affected by the formation of the cyclic ring. The NH…O H-bond of the less stable b isomer is not affected.

Table 1. Positions and suggested vibrational and isomer assignments of the transitions observed in the IRPD spectra of $H^+Ox\text{-}W_n$ (n=1-4) and $H^+Ox\text{-}W_n\text{-}N_2$ (n=1-2) clusters compared to frequencies of the most stable isomers calculated at the B3LYP-D3/aug-cc-pVTZ level. All values are given in cm^{-1}. For comparison, spectral data of W_n with n≤2 are provided.

	exp (cm^{-1})	calc (cm^{-1}) [a]	assignment	isomer
W	3756 [b]	3757 (63)	ν_3	
	3657 [b]	3658 (5)	ν_1	
W_2	3746 [c]	3749 (84)	ν_3	
	3735 [c]	3730 (86)	ν_f	
	3654 [c]	3653 (10)	ν_1	
	3601 [c]	3542 (341)	ν_{OH} [b]	
Ox	3168 [d]	3170 (0.4)	ν_{CH}	Ox
	3148 [d]	3137 (2)	ν_{CH}	
		3144 (0.9)	ν_{CH}	
H^+Ox	3444±3 [e]	3446 (202)	ν_{NH} [f]	$H^+Ox(N)$
	3205±5 [e]	3181 (27)	ν_{CH}	
	3180±10 [e]	3161 (40)	ν_{CH}	
	3170±10 [e]	3149 (69)	ν_{CH}	
$H^+Ox\text{-}W$	A 3720	3728 (151)	ν_3	$H^+Ox\text{-}W(H)$
	B 3625	3642 (56)	ν_1	
	X 3230		$2\beta_{OH}$	
	E 3179	3184 (16)	ν_{CH}	
	E 3179	3163 (31)	ν_{CH}	
	E 3179	3155 (57)	ν_{CH}	
	F1 3095	2883 (1840)	ν_{NH} [b]	
	F2 2969			
	F3 2833			
$H^+Ox\text{-}W\text{-}N_2$	A 3711	3706 (195)	ν_3	$H^+Ox\text{-}W(H)\text{-}N_2(H)$
	B 3610	3576 (383)	ν_1	
	X 3230		$2\beta_{OH}$	
	E 3178	3184 (15)	ν_{CH}	
	E 3178	3164 (30)	ν_{CH}	
	E 3178	3156 (54)	ν_{CH}	
	F 2970	2785 (2209)	ν_{NH} [b]	
$H^+Ox\text{-}W_2$	A 3745	3739 (124)	ν_3	$H^+Ox\text{-}W_2(H)$
	C 3705	3712 (115)	ν_f	
	B 3649	3651 (31)	ν_1	
	D 3338	3267 (1023)	ν_{OH} [b]	
	X 3247		$2\beta_{OH}$	
	E 3179	3185 (14)	ν_{CH}	
	E 3179	3164 (27)	ν_{CH}	
	E 3179	3158 (48)	ν_{CH}	
		2554 (2853)	ν_{NH} [b]	
$H^+Ox\text{-}W_2\text{-}N_2$	A 3742	3741 (121), 3739 (122)	ν_3	$H^+Ox\text{-}W_2(H)\text{-}N_2(H1)$, $H^+Ox\text{-}W_2(H)\text{-}N_2(\pi)$
	C1 3707	3712 (116)	ν_f	$H^+Ox\text{-}W_2(H)\text{-}N_2(\pi)$
	C2 3667	3643 (422)	ν_f	$H^+Ox\text{-}W_2(H)\text{-}N_2(H1)$
	B 3657	3653 (42), 3650 (30)	ν_1	$H^+Ox\text{-}W_2(H)\text{-}N_2(H1)$, $H^+Ox\text{-}W_2(H)\text{-}N_2(\pi)$

	D 3312	3301 (984), 3278 (968)	ν_{OH}[b]	H^+Ox-W_2(H)-N_2(H1), H^+Ox-W_2(H)-N_2(π)
	X 3253		$2\beta_{OH}$	H^+Ox-W_2(H)-N_2(H1), H^+Ox-W_2(H)-N_2(π)
	E 3174	3185 (14), 3186 (13)	ν_{CH}	H^+Ox-W_2(H)-N_2(H1), H^+Ox-W_2(H)-N_2(π)
	E 3174	3164 (26), 3165 (25)	ν_{CH}	
	E 3174	3159 (46), 3161 (47)	ν_{CH}	
H^+Ox-W_3	A 3743	3744 (230),[f] 3745 (115)	ν_3	H^+Ox-W_3(b), H^+Ox-W_3(l)
	C 3707	3717 (84)	ν_f	H^+Ox-W_3(l)
	C 3707	3715 (115)	ν_f	H^+Ox-W_3(l)
	B 3654	3654 (47),[f] 3654 (23)	ν_1	H^+Ox-W_3(b), H^+Ox-W_3(l)
	D1 3348	3384 (1362), 3374 (702)	ν_{OH}[b]	H^+Ox-W_3(b), H^+Ox-W_3(l)
	D1 3348	3349 (521)	ν_{OH}[b]	H^+Ox-W_3(b)
	X 3242		$2\beta_{OH}$	H^+Ox-W_3(b), H^+Ox-W_3(l)
	E 3178	3185 (12), 3185 (12)	ν_{CH}	H^+Ox-W_3(b), H^+Ox-W_3(l)
	E 3178	3164 (22), 3164 (24)	ν_{CH}	
	E 3178	3160 (40), 3159 (45)	ν_{CH}	
	D2 3050	3046 (1548)	ν_{OH}[b]	H^+Ox-W_3(l)
H^+Ox-W_4	A 3741	3749 (113), 3742 (121)	ν_3	H^+Ox-W_4(b), H^+Ox-W_4(c1)
	A 3741	3745 (112)	ν_3	H^+Ox-W_4(b)
	C 3715	3722 (90), 3726 (121)	ν_f	H^+Ox-W_4(b), H^+Ox-W_4(c1)
	C 3715	3709 (110)	ν_f	H^+Ox-W_4(c1)
	C 3715	3692 (95)	ν_f	H^+Ox-W_4(c1)
	B 3651	3657 (22), 3653 (29)	ν_1	H^+Ox-W_4(b), H^+Ox-W_4(c1)
	B 3651	3655 (22)	ν_1	H^+Ox-W_4(b)
	Y 3567	3562 (357)	ν_{OH}[b]	H^+Ox-W_4(c2)
	D1 3427	3401 (502), 3428 (414)	ν_{OH}[b]	H^+Ox-W_4(b), H^+Ox-W_4(c1)
	D1 3427	3379 (1113)	ν_{OH}[b]	H^+Ox-W_4(b)
	D2/X 3247	3161 (1450), 3325 (945)	ν_{OH}[b]/$2\beta_{OH}$	H^+Ox-W_4(b), H^+Ox-W_4(c1)
	D2 3247	3194 (1179)	ν_{OH}[b]	H^+Ox-W_4(c1)
	E 3180	3185 (10), 3186 (16)	ν_{CH}	H^+Ox-W_4(b), H^+Ox-W_4(c1)
	E 3180	3164 (15), 3164 (21)	ν_{CH}	H^+Ox-W_4(b), H^+Ox-W_4(c1)
	E 3180	3160 (46)	ν_{CH}	H^+Ox-W_4(b)
	H 3084	3027 (364)	ν_{CH}[b]	H^+Ox-W_4(c1)

[a] IR intensities (in km/mol) are listed in parentheses.

[b] Ref. 71.

[c] Ref. 80, 81, 82.

[d] Ref. 46.

[e] Ref. 60.

[f] The intensities of the two nearly degenerate modes are added.

References

(1) Pal, S. K.; Zewail, A. H. Dynamics of Water in Biological Recognition. *Chem. Rev.* **2004**, *104*, 2099–2123.

(2) Perrin, C. L.; Nielson, J. B. "Strong" Hydrogen Bonds in Chemistry and Biology. *Annu. Rev. Phys. Chem.* **1997**, *48*, 511–544.

(3) Zhong, D.; Pal, S. K.; Zewail, A. H. Biological Water: A Critique. *Chem. Phys. Lett.* **2011**, *503*, 1–11.

(4) Chaplin, M. Do We Underestimate the Importance of Water in Cell Biology? *Nat. Rev. Mol. Cell Biol.* **2006**, *7*, 861–866.

(5) Levy, Y.; Onuchic, J. N. Water Mediation in Protein Folding and Molecular Recognition. *Annu. Rev. Biophys. Biomol. Struct.* **2006**, *35*, 389–415.

(6) Ball, P. Water as an Active Constituent in Cell Biology. *Chem. Rev.* **2008**, *108*, 74–108.

(7) Bagchi, B. Water Dynamics in the Hydration Layer around Proteins and Micelles. *Chem. Rev.* **2005**, *105*, 3197–3219.

(8) Rasaiah, J. C.; Garde, S.; Hummer, G. Water in Nonpolar Confinement: From Nanotubes to Proteins and Beyond. *Annu. Rev. Phys. Chem.* **2008**, *59*, 713–740.

(9) Mattos, C. Protein-Water Interactions in a Dynamic World. *Trends Biochem. Sci.* **2002**, *27*, 203–208.

(10) Dopfer, O.; Fujii, M. Probing Solvation Dynamics around Aromatic and Biological Molecules at the Single-Molecular Level. *Chem. Rev.* **2016**, *116*, 5432–5463.

(11) Nandi, N.; Bhattacharyya, K.; Bagchi, B. Dielectric Relaxation and Solvation Dynamics of Water in Complex Chemical and Biological Systems. *Chem. Rev.* **2000**, *100*, 2013–2045.

(12) Eisenthal, K. B. Liquid Interfaces. *Acc. Chem. Res.* **1993**, *26*, 636–643.

(13) Bizzarri, A. R.; Cannistraro, S. Molecular Dynamics of Water at the Protein-Solvent Interface. *J. Phys. Chem. B* **2002**, *106*, 6617–6633.

(14) Makarov, V.; Pettitt, B. M.; Feig, M. Solvation and Hydration of Proteins and Nucleic Acids: A Theoretical View of Simulation and Experiment. *Acc. Chem. Res.* **2002**, *35*, 376–384.

(15) Li, Z.; Lazaridis, T. The Effect of Water Displacement on Binding Thermodynamics: Concanavalin A. *J. Phys. Chem. B* 2005, *109*, 662–670.

(16) Ben-Naim, A. Molecular Recognition - Viewed through the Eyes of the Solvent. *Biophys. Chem.* **2002**, *101–102*, 309–319.

(17) de Vries, M. S.; Hobza, P. Gas-Phase Spectroscopy of Biomolecular Building Blocks. *Annu. Rev. Phys. Chem.* **2006**, *58*, 585–612.

(18) Boyarkin, O. V. Cold Ion Spectroscopy for Structural Identifications of Biomolecules. *Int. Rev. Phys. Chem.* **2018**, *37*, 559–606.

(19) Nagornova, N. S.; Rizzo, T. R.; Boyarkin, O. V. Exploring the Mechanism of IR-UV Double-Resonance for Quantitative Spectroscopy of Protonated Polypeptides and Proteins. *Angew. Chem. Int. Ed*. 2013, *52*, 6002–6005.

(20) Rizzo, T. R.; Stearns, J. A.; Boyarkin, O. V. Spectroscopic Studies of Cold, Gas-Phase Biomolecular Ions. *Int. Rev. Phys. Chem.* **2009**, *28*, 481–515.

(21) Müller-Dethlefs, K.; Dopfer, O.; Wright, T. G. ZEKE Spectroscopy of Complexes and Clusters. *Chem. Rev.* **1994**, *94*, 1845–1871.

(22) Duncan, M. A. Spectroscopy of Metal Ion Complexes: Gas-Phase Models for Solvation. *Annu. Rev. Phys. Chem.* **2002**, *48*, 69–93.

(23) Bieske, E. J. Spectroscopic Studies of Anion Complexes and Clusters: A Microscopic Approach to Understanding Anion Solvation. *Chem. Soc. Rev.* **2003**, *32*, 231–237.

(24) Castleman, A. W.; Keesee, R. G. Ionic Clusters. *Chem. Rev.* **1986**, *86*, 589–618.

(25) Bieske, E. J.; Dopfer, O. High-Resolution Spectroscopy of Cluster Ions. *Chem. Rev.* **2000**, *100*, 3963–3998.

(26) Müller-Dethlefs, K.; Hobza, P. Noncovalent Interactions: A Challenge for Experiment and Theory. *Chem. Rev.* **2000**, *100*, 143–168.

(27) Bagley, M. C.; Dale, J. W.; Merritt, E. A.; Xiong, X. Thiopeptide Antibiotics. *Chem. Rev.* **2005**, *105*, 685–714.

(28) Chiu, M. L.; Folcher, M.; Katoh, T.; Puglia, A. M.; Vohradsky, J.; Yun, B.-S.; Seto, H.; Thompson, C. J. Broad Spectrum Thiopeptide Recognition Specificity of the Streptomyces lividans TipAL Protein and Its Role in Regulating Gene Expression. *J. Biol. Chem.* **1999**, *274*, 20578–20586.

(29) Gürsoy, A.; Demirayak, Ş.; Çapan, G.; Erol, K.; Vural, K. Synthesis and Preliminary Evaluation of New 5-Pyrazolinone Derivatives as Analgesic Agents. *Eur. J. Med. Chem.* **2000**, *35*, 359–364.

(30) Bull, J. A.; Balskus, E. P.; Horan, R. A. J.; Langner, M.; Ley, S. V. Total Synthesis of Potent Antifungal Marine Bisoxazole Natural Products Bengazoles A and B. *Chem. Eur. J.* **2007**, *13*, 5515–5538.

(31) Boyd, R. E.; Press, J. B.; Rasmussen, C. R.; Raffa, R. B.; Codd, E. E.; Connelly, C. D.; Bennett, D. J.; Kirifides, A. L.; Gardocki, J. F.; Reynolds, B.; et al. α_2 Adrenoceptor Agonists as Potential Analgesic Agents. 1. (Imidazolylmethyl)Oxazoles and -Thiazoles . *J. Med. Chem*. 1999, *42*, 5064–5071.

(32) Kempf, D. J.; Sham, H. L.; Marsh, K. C.; Flentge, C. A.; Betebenner, D.; Green, B. E.; McDonald E.; Vasavanonda, S.; Saldivar, A.; Wideburg, N. E.; et al. Discovery of Ritonavir, a Potent Inhibitor of HIV Protease with High Oral Bioavailability and Clinical Efficacy. *J. Med. Chem.* **1998**, *41*, 602–617.

(33) Dinarello, C. A. Anti-Inflammatory Agents: Present and Future. *Cell* **2010**, *140*, 935–950.

(34) Li, Y.-M.; Milne, J. C.; Madison, L. L.; Kolter, R.; Walsh, C. T. From Peptide Precursors to Oxazole and Thiazole-Containing Peptide Antibiotics: Microcin B17 Synthase. *Science* **2002**, *274*, 1188–1193.

(35) Vijaya Kumar, E. K. S.; Kenia, J.; Mukhopadhyay, T.; Nadkarni, S. R. Methylsulfomycin I, a New Cyclic Peptide Antibiotic from a Streptomyces Sp. HIL Y-9420704. *J. Nat. Prod.* **1999**, *62*, 1562–1564.

(36) Sasahara, K.; Shimokawa, Y.; Hirao, Y.; Koyama, N.; Kitano, K.; Shibata, M.; Umehara, K. Pharmacokinetics and Metabolism of Delamanid, a Novel Anti-Tuberculosis Drug, in Animals and Humans: Importance of Albumin Metabolism In Vivo. *Drug Metab. Dispos.* **2015**, *43*, 1267–1276.

(37) Portmann, C.; Blom, J. F.; Kaiser, M.; Brun, R.; Jüttner, F.; Gademann, K. Isolation of Aerucyclamides C and D and Structure Revision of Microcyclamide 7806A: Heterocyclic Ribosomal Peptides from Microcystis Aeruginosa PCC 7806 and Their Antiparasite Evaluation. *J. Nat. Prod.* **2008**, *71*, 1891–1896.

(38) Andersson, I. E.; Batsalova, T.; Dzhambazov, B.; Edvinsson, L.; Holmdahl, R.; Kihlberg, J.; Linusson, A. Oxazole-Modified Glycopeptides That Target Arthritis-Associated Class II MHC Aq and DR4 Proteins. *Org. Biomol. Chem.* **2010**, *8*, 2931–2940.

(39) Jin, Z. Muscarine, Imidazole, Oxazole and Thiazole Alkaloids. *Nat. Prod. Rep.* **2016**, *33*, 1268–1317.

(40) Ceide, S. C.; Trembleau, L.; Haberhauer, G.; Somogyi, L.; Lu, X.; Bartfai, T.; Rebek, J. Synthesis of Galmic: A Nonpeptide Galanin Receptor Agonist. *Proc. Natl. Acad. Sci.* **2004**, *101*, 16727–16732.

(41) Haberhauer, G.; Drosdow, E.; Oeser, T.; Rominger, F. Structural Investigation of Westiellamide Analogues. *Tetrahedron* **2008**, *64*, 1853–1859.

(42) Siodłak, D.; Staś, M.; Broda, M. A.; Bujak, M.; Lis, T. Conformational Properties of Oxazole-Amino Acids: Effect of the Intramolecular N-H···N Hydrogen Bond. *J. Phys. Chem. B* **2014**, *118*, 2340–2350.

(43) Haberhauer, G.; Pintér, Á.; Oeser, T.; Rominger, F. Synthesis and Structural Investigation of C_4- and C_2-Symmetric Molecular Scaffolds Based on Imidazole Peptides. *Eur. J. Org. Chem.* **2007**, 1779–1792.

(44) Xia, X.; Tang, W.; He, S.; Kang, J.; Ma, H.; Li, J. Mechanism of Metamifop Inhibition of the Carboxyltransferase Domain of Acetyl-Coenzyme A Carboxylase in Echinochloa Crus-Galli. *Sci. Rep.* **2016**, *6*, 1–10.

(45) Borello, E.; Zecchina, A.; Appiano, A. Infra-Red Spectra of Oxazole and Its Alkyl Derivatives−I. **1966**, *22*, 977-983

(46) Sbrana, G.; Castellucci, E.; Ginanneschi, M. Infra-Red and Raman Spectra of Five-Membered Heterocyclic Molecules—Oxazole and Thiazole. *Spectrochim. Acta A* **1967**, *23*, 751–758.

(47) Hegelund, F.; Larsen, R. W.; Palmer, M. H. High-Resolution Infrared and Theoretical Study of Gaseous Oxazole in the 600-1400 Cm^{-1} Region. *J. Mol. Spectrosc.* **2007**, *241*, 26–44.

(48) Civcir, P. Ü.; Kurtay, G.; Sarıkavak, K. Experimental and Theoretical Investigation of New Furan and Thiophene Derivatives Containing Oxazole, Isoxazole, or Isothiazole Subunits. *Struct. Chem.* **2017**, *28*, 773–790.

(49) Kaur, D.; Khanna, S. Intermolecular Hydrogen Bonding Interactions of Furan, Isoxazole and Oxazole with Water. *Comput. Theor. Chem.* **2011**, *963*, 71–75.

(50) Palmer, M. H. Comparison of Theoretical and Experimental Studies of Infrared Spectral Data for the 5-Membered Ring Heterocycles. *J. Mol. Struct.* **2007**, *834–836*, 113–128.

(51) Cao, J.; Xie, Z. -Z.; Yu, X. Excited-State Dynamics of Oxazole: A Combined Electronic Structure Calculations and Dynamic Simulations Study. *Chem. Phys.* **2016**, *474*, 25–35.

(52) Kumar, A.; Sheridan, J.; Stiefvater, O. L. The Microwave Spectrum of Oxazole I. The Complete Structure by DRM Microwave Spectroscopy. *Z. Naturforsch. A* **1978**, *33*, 145–152.

(53) Turchi, I. J.; Dewar, M. J. S. The Chemistry of Oxazoles. *Chem. Rev.* **1975**, *75*, 389–437.

(54) Han, S.; Kang, T. Y.; Choi, S.; Choi, K.-W.; Baek, S. J.; Lee, S.; Kim, S. K. One-Photon Ionization Spectroscopy of Jet-Cooled Oxazole and Thiazole: The Role of Oxygen and Sulfur in the π-Conjugation of Heterocyclic Compounds. *Phys. Chem. Chem. Phys.* **2008**, *10*, 3883–3887.

(55) Palmer, M. H.; Findlay, R. H.; Egdell, R. G. The Electronic Structure of Heteroaromatic Molecules; Ab Initio Calculations and Photoelectron Spectra for the Isomeric Oxazoles and Some Oxadiazoles. *J. Mol. Struct.* **1977**, *40*, 191–210.

(56) Culberson, L. M.; Blackstone, C. C.; Wysocki, R.; Sanov, A. Selective Deprotonation of Oxazole and Photoelectron Imaging of the Oxazolide Anion. *Phys. Chem. Chem. Phys.* **2014**, *16*, 527–532.

(57) Mátyus, P.; Fuji, K.; Tanaka, K. Density Functional Calculations on Heterocyclic Compounds. Part 1. Studies of Protonation of 5- and 6-Membered Nitrogen Heterocyclics. *Tetrahedron* **1994**, *50*, 2405–2414.

(58) Jursic, B. S. Density Functional Theory Study of Ethene and Acetylene Addition to Oxazole and Protonated Oxazole. *J. Chem. Soc. Perkin Trans. 2* **1996**, 1021-1026.

(59) Hunter, E. P. L.; Lias, S. G. Evaluated Gas Phase Basicities and Proton Affinities of Molecules: An Update. *J. Phys. Chem. Ref. Data* **1998**, *27*, 413–656.

(60) Chatterjee, K.; Dopfer, O. Unraveling the Protonation Site of Oxazole and Solvation with Hydrophobic Ligands by Infrared Photodissociation Spectroscopy. *Phys. Chem. Chem. Phys.* **2019,** *21***,** 15157-15166.

(61) Dopfer, O. Spectroscopic and Theoretical Studies of CH_3^+-Rg_n Clusters (Rg=He, Ne, Ar): From Weak Intermolecular Forces to Chemical Reaction Mechanisms. *Int. Rev. Phys. Chem.* **2003**, *22*, 437–495.

(62) Dopfer, O. IR Spectroscopy of Microsolvated Aromatic Cluster Ions: Ionization-Induced Switch in Aromatic Molecule-Solvent Recognition. *Z. Phys. Chem.* **2005**, *219*, 125–168.

(63) Frisch, M. J. et al. *Gaussian 09*, *D.01,* Gaussian, Inc., Wallingford, CT, USA 2009.

(64) Chatterjee, K.; Matsumoto, Y.; Dopfer, O. Aromatic Charge Resonance Interaction Probed by Infrared Spectroscopy. *Angew. Chem. Int. Ed.* **2019**, *58*, 3351–3355.

(65) Chatterjee, K.; Dopfer, O. Infrared Signatures of Protonated Benzonitrile. *Astrophys. J.* **2018**, *865*, 114.

(66) Klyne, J.; Dopfer, O. Microhydration of Protonated 5-Hydroxyindole Revealed by Infrared Spectroscopy. *Phys. Chem. Chem.*

Phys. **2019**, *21*, 2706–2718.

(67) Klyne, J.; Miyazaki, M.; Fujii, M.; Dopfer, O. Sequential Microhydration of Cationic 5-Hydroxyindole ($5HI^+$): Infrared Photodissociation Spectra of $5HI^+$–W_n Clusters (W=H_2O, n≤4). *Phys. Chem. Chem. Phys.* **2018**, *20*, 3092–3108.

(68) Chatterjee, K.; Dopfer, O. Microhydration of PAH^+ Cations: Evolution of Hydration Network in Naphthalene$^+$-$(H_2O)_n$ Clusters (n≤5). *Chem. Sci.* **2018**, *9*, 2301-2318.

(69) Schütz, M.; Matsumoto, Y.; Bouchet, A.; Öztürk, M.; Dopfer, O. Microsolvation of the Pyrrole Cation (Py^+) with Nonpolar and Polar Ligands: Infrared Spectra of Py^+-L_n with L = Ar, N_2, and H_2O (n≤3). *Phys. Chem. Chem. Phys.* **2017**, *19*, 3970–3986.

(70) Rocher-Casterline, B. E.; Ch'ng, L. C.; Mollner, A. K.; Reisler, H. Communication: Determination of the Bond Dissociation Energy (D_0) of the Water Dimer, $(H_2O)_2$, by Velocity Map Imaging. *J. Chem. Phys.* **2011**, *134*, 211101.

(71) Herzberg, G. *Molecular Spectra and Molecular Structure. II. Infrared and Raman Spectra of Polyatomic Molecules*; Krieger Publishing Company, Malabar, Florida, 1991.

(72) Glendening, E. D.; Badenhoop, J. K.; Reed, A. E.; Carpenter, J. E.; Bohmann, J. A.; Morales, C. M.; Landis, C. R.; Weinhold, F. NBO 6.0, Theoretical Chemistry. University of Wisconsin, Madison 2013.

(73) Reed, A. E.; Curtiss, L. A.; Weinhold, F. Intermolecular Interactions from a Natural Bond Orbital, Donor-Acceptor Viewpoint. *Chem. Rev.* **1988**, *88*, 899–926.

(74) Contreras-García, J.; Johnson, E. R.; Keinan, S.; Chaudret, R.; Piquemal, J. P.; Beratan, D. N.; Yang, W. NCIPLOT: A Program for Plotting Noncovalent Interaction Regions. *J. Chem. Theory Comput.* **2011**, *7*, 625–632.

(75) Johnson, E. R.; Keinan, S.; Mori Sánchez, P.; Contreras García, J.; Cohen, A. J.; Yang, W. NCI : Revealing Non-Covalent Interactions. *J. Am. Chem. Soc.* **2010**, *132*, 6498–6506.

(76) Császár, A. G.; Czakó, G.; Furtenbacher, T.; Tennyson, J.; Szalay, V.; Shirin, S. V.; Zobov, N. F.; Polyansky, O. L. On Equilibrium Structures of the Water Molecule. *J. Chem. Phys.* **2005**, *122,* 214305.

(77) Klyne, J.; Schmies, M.; Miyazaki, M.; Fujii, M.; Dopfer, O. Stepwise Microhydration of Aromatic Amide Cations: Water Solvation Networks Revealed by the Infrared Spectra of Acetanilide$^+$–$(H_2O)_n$ Clusters (n≤3). *Phys. Chem. Chem. Phys.* **2018**, *20*, 3148–3164.

(78) Klyne, J.; Schmies, M.; Fujii, M.; Dopfer, O. Stepwise Microhydration of Aromatic Amide Cations: Formation of Water Solvation Network Revealed by Infrared Spectra of Formanilide$^+$–$(H_2O)_n$ Clusters (n≤5). *J. Phys. Chem. B* **2015**, *119*, 1388–1406.

(79) Goebbert, D. J.; Wenthold, P. G. Water Dimer Proton Affinity from the Kinetic Method: Dissociation Energy of the Water Dimer. *Eur. J. Mass Spectrom.* **2004**, *10*, 837–845.

(80) Kuyanov-Prozument, K.; Choi, M. Y.; Vilesov, A. F. Spectrum and Infrared Intensities of OH-Stretching Bands of Water Dimers. *J. Chem. Phys.* **2010**, *132*, 14304.

(81) Huisken, F.; Kaloudis, M.; Kulcke, A. Infrared Spectroscopy of Small Size-selected Water Clusters. *J. Chem. Phys.* **1996**, *104*, 17–25.

(82) Huang, Z. S.; Miller, R. E. High-resolution Near-infrared Spectroscopy of Water Dimer. *J. Chem. Phys.* **1989**, *91*, 6613–6631.

(83) Courty, A.; Mons, M.; Le Calvé, J.; Piuzzi, F.; Dimicoli, I. Chemistry of Aromatic Cations on Water Clusters: Magic Numbers as a Mass Spectroscopic Diagnosis of Reactivity. *J. Phys. Chem. A* **1997**, *101*, 1445–1450.

(84) Bing, D.; Hamashima, T.; Tsai, C.-W.; Fujii, A.; Kuo, J.-L. Proton Location in $(CH_3)_3N$-H^+-$(CH_3OH)_n$: A Theoretical and Infrared Spectroscopy Study. *Chem. Phys.* **2013**, *421*, 1-9.

(85) Chatterjee, K.; Dopfer, O. Infrared Spectroscopy Hydrated Polycyclic Aromatic Hydroarbon Cations: Naphthalene+-Water. *Phys. Chem. Chem. Phys.* **2017**, *19*, 32262–32271.

(86) Cheng, T. C.; Bandyopadhyay, B.; Mosley, J. D.; Duncan, M. A. IR Spectroscopy of Protonation in Benzene-Water Nanoclusters: Hydronium, Zundel, and Eigen at a Hydrophobic Interface. *J. Am. Chem. Soc.* **2012**, *134*, 13046-13055.

(87) Kryachko, E. S.; Nguyen, M. T. Low Energy Barrier Proton Transfer in Protonated Benzene-Water Complex. *J. Phys. Chem. A* **2001**, *105*, 153-155.

(88) Solcà, N.; Dopfer, O. IR Spectrum of the Benzene-Water Cation: Direct Evidence for a Hydrogen-Bonded Charge-Dipole Complex. *Chem. Phys. Lett.* **2001**, *347*, 59-64.

(89). Tanabe, K.; Miyazaki, M.; Schmies, M.; Patzer, A.; Schütz, M.; Sekiya, H.; Sakai, M.; Dopfer, O.; Fujii, M. Watching Water Migration around a Peptide Bond. *Angew. Chem. Int. Ed.* **2012**, *51*, 6604-6607.

(90) Nakamura, T.; Schmies, M.; Patzer, A.; Miyazaki, M.; Ishiuchi, S.; Weiler, M.; Dopfer, O.; Fujii, M. Solvent Migration in Microhydrated Aromatic Aggregates: Ionization-Induced Site Switching in the 4-Aminobenzonitrile Water Cluster. *Chem. Eur. J.* **2014**, *20*, 2031-2039.

(91) Wohlgemuth, M.; Miyazaki, M.; Weiler, M.; Sakai, M.; Dopfer, O.; Fujii, M.; Mitrić, R. Solvation Dynamics of a Single Water Molecule Probed by Infrared Spectra-Theory Meets Experiment. *Angew. Chem. Int. Ed.* **2014**, *54*, 14601-14604.

(92) Wohlgemuth, M.; Miyazaki, M.; Tsukada, K.; Weiler, M.; Dopfer, O.; Fujii, M.; Mitrić, R. Deciphering Environment Effects in Peptide Bond Solvation Dynamics by Experiment and Theory. *Phys. Chem. Chem. Phys.* **2017**, *19*, 22564-22572.

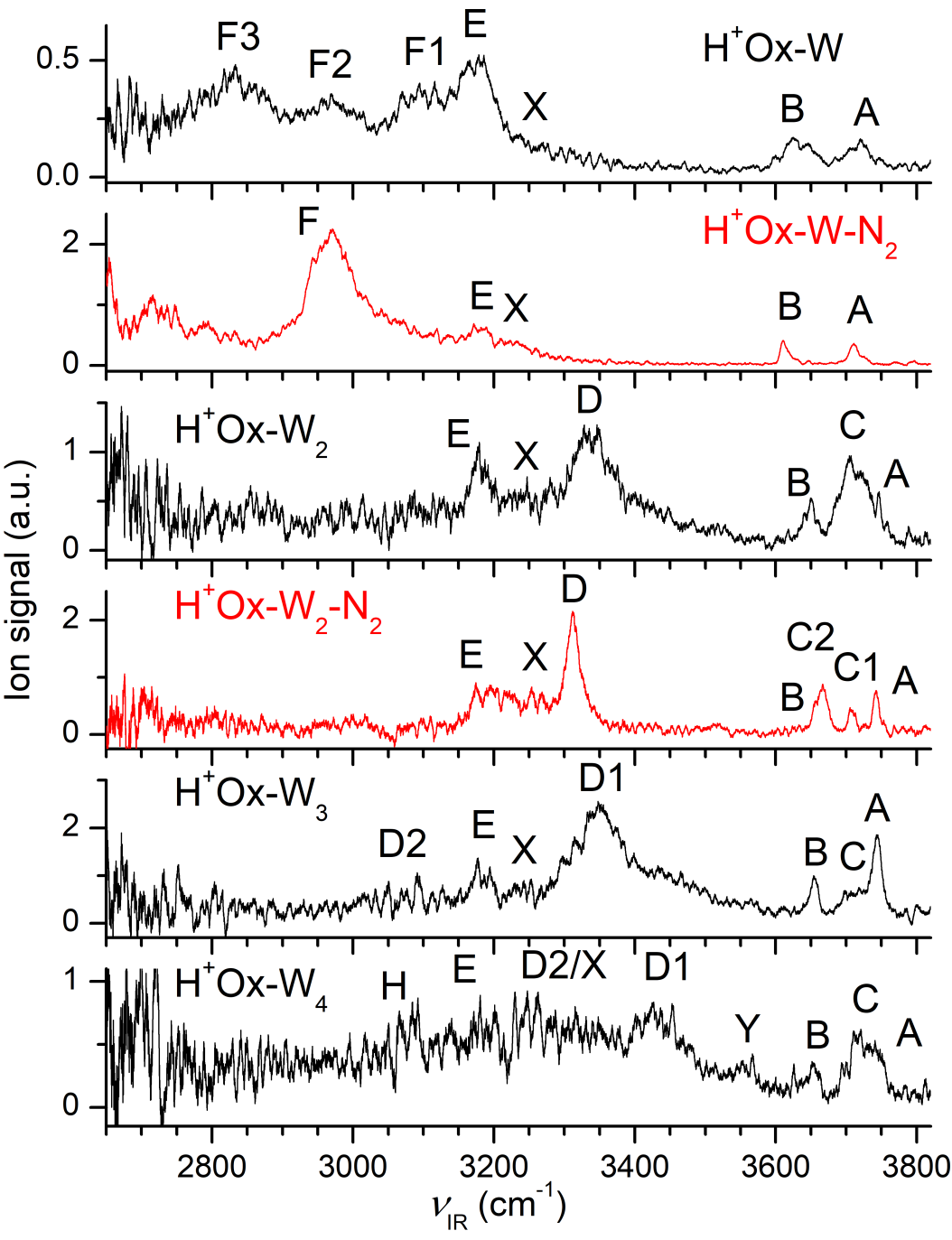
F3
F2
F1
E
X
B
A
H+Ox-W
F
E
X
B
A
H+Ox-W-N2
H+Ox-W2
E
X
D
B
C
A
H+Ox-W2-N2
E
X
D
B
C2
C1
A
H+Ox-W3
D2
E
X
D1
B
C
A
H+Ox-W4
H
E
D2/X
D1
Y
B
C
A
Ion signal (a.u.)
0.5
0.0
2
0
1
0
2
0
2
0
1
0
2800
3000
3200
3400
3600
3800
νIR (cm-1)

Figure 1

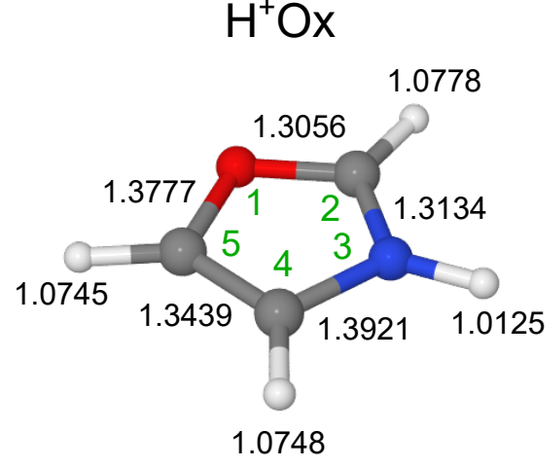
H+Ox
1.0778
1.3056
1.3777
1
2
1.3134
5
3
4
1.0745
1.3439
1.3921
1.0125
1.0748

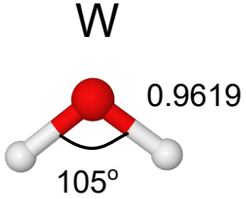
W
0.9619
105°

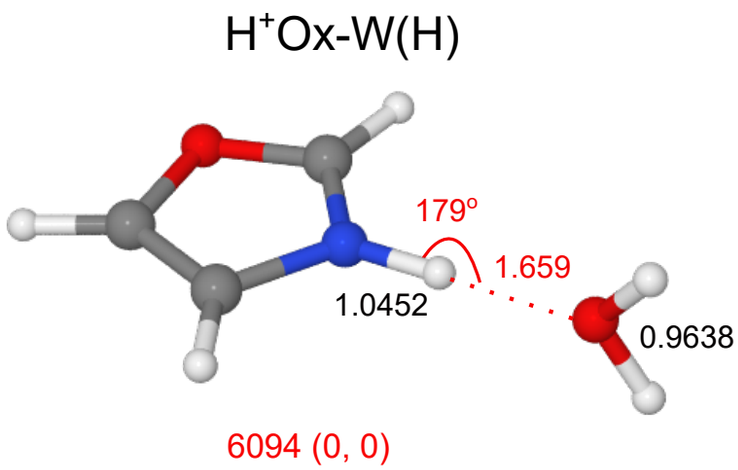
H+Ox-W(H)
179°
1.659
1.0452
0.9638
6094 (0, 0)

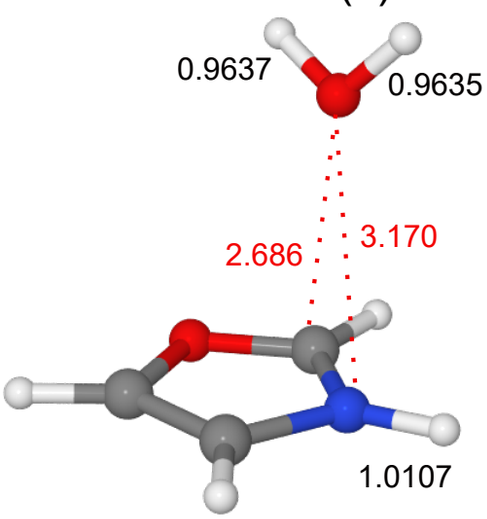
H+Ox-W(π)
0.9637
0.9635
2.686
3.170
1.0107
3334 (2759, 2536)

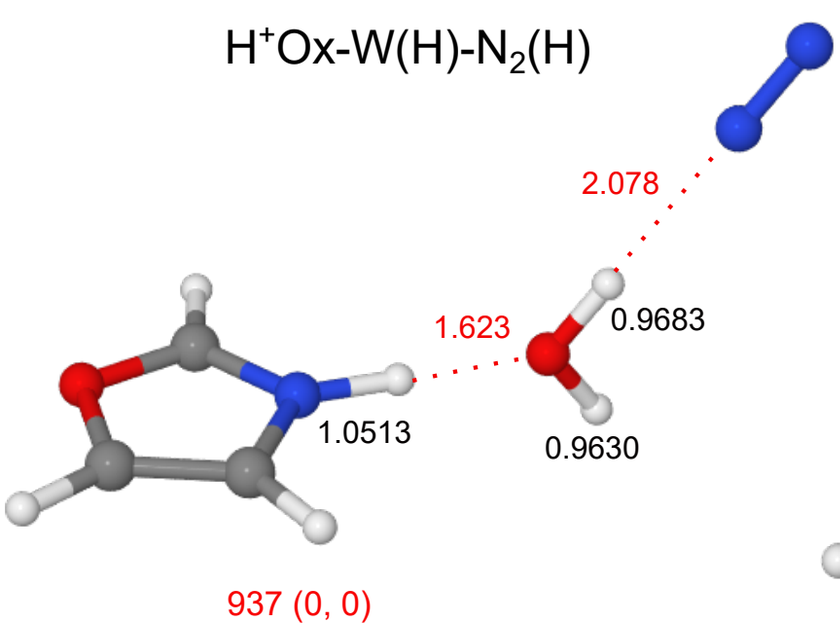
H+Ox-W(H)-N2(H)
2.078
1.623
0.9683
1.0513
0.9630
937 (0, 0)

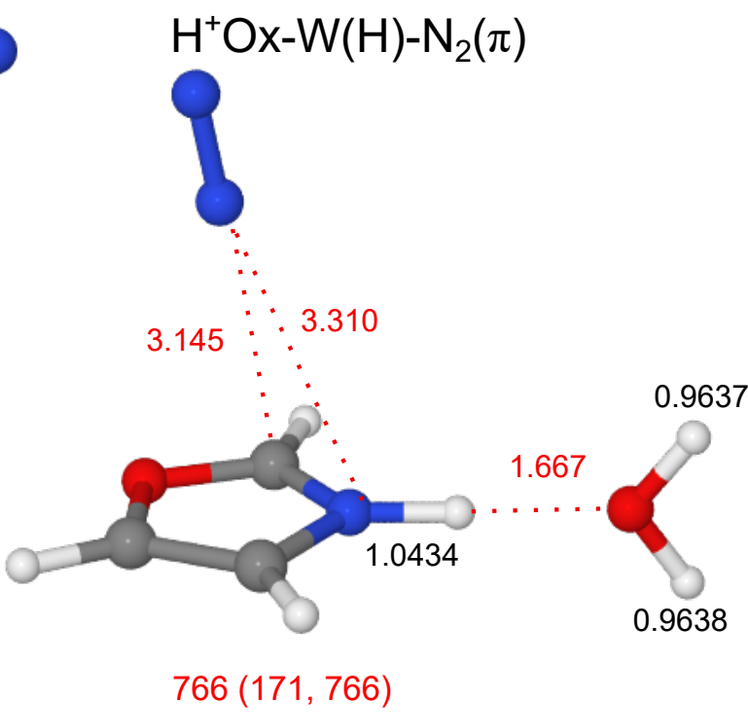
H+Ox-W(H)-N2(π)
3.145
3.310
0.9637
1.667
1.0434
0.9638
766 (171, 766)

Figure 2

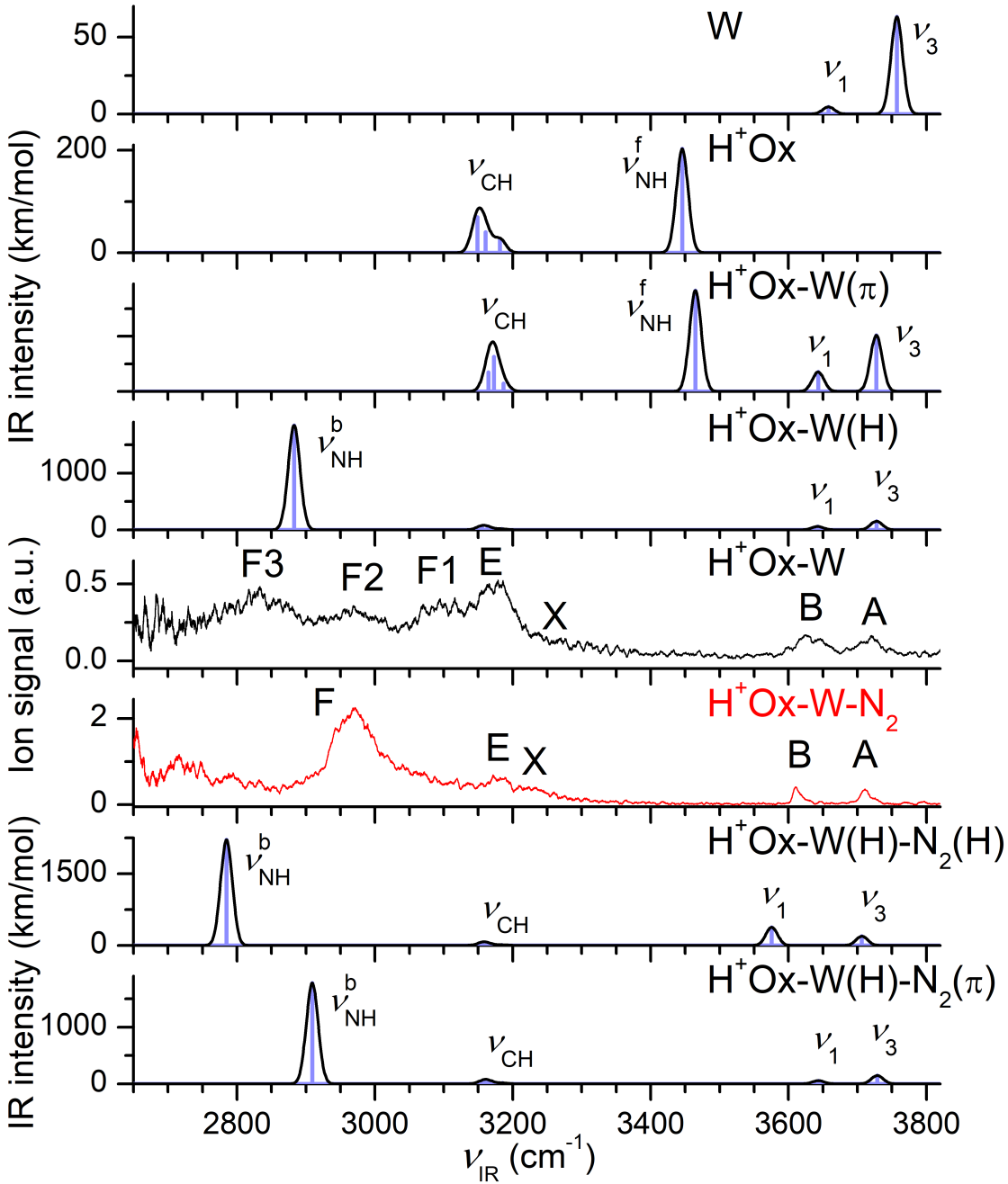
W
ν_1
ν_3
H$^+$Ox
ν_{CH}
ν^f_{NH}
H$^+$Ox-W(π)
H$^+$Ox-W(H)
ν^b_{NH}
H$^+$Ox-W
F3
F2
F1
E
X
B
A
H$^+$Ox-W-N$_2$
F
H$^+$Ox-W(H)-N$_2$(H)
H$^+$Ox-W(H)-N$_2$(π)
IR intensity (km/mol)
Ion signal (a.u.)
ν_{IR} (cm^{-1})

Figure 3

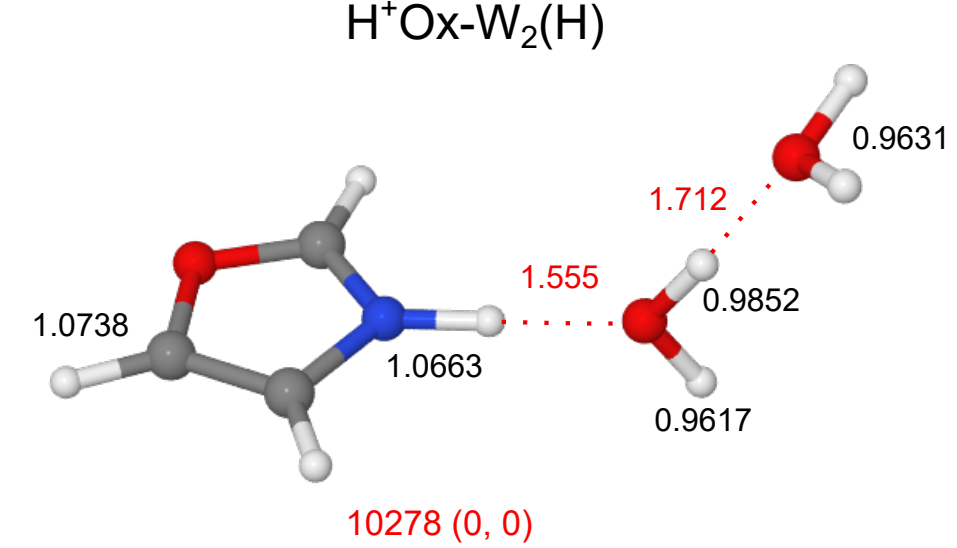
H+Ox-W2(H)
0.9631
1.712
1.555
0.9852
1.0738
1.0663
0.9617
10278 (0, 0)

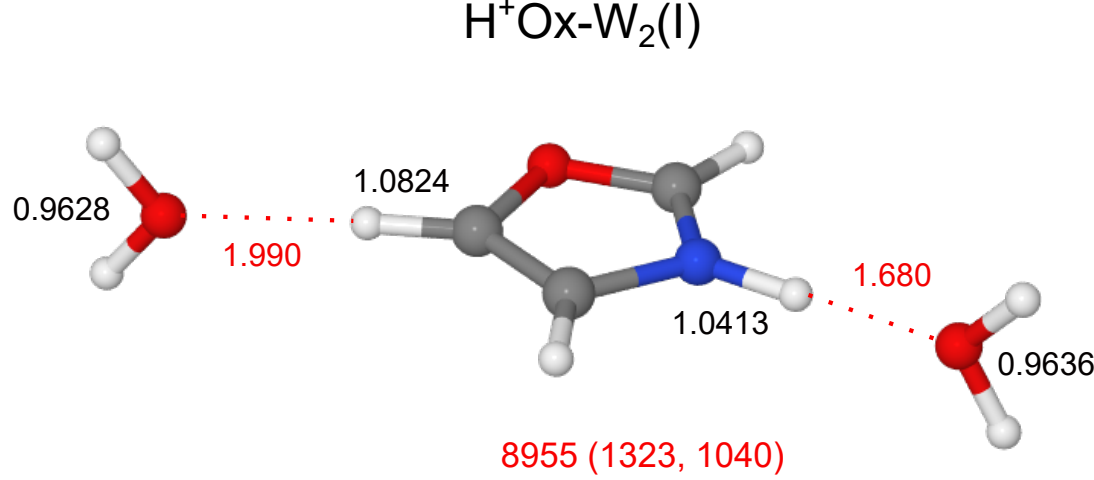
H+Ox-W2(I)
0.9628
1.990
1.0824
1.0413
1.680
0.9636
8955 (1323, 1040)

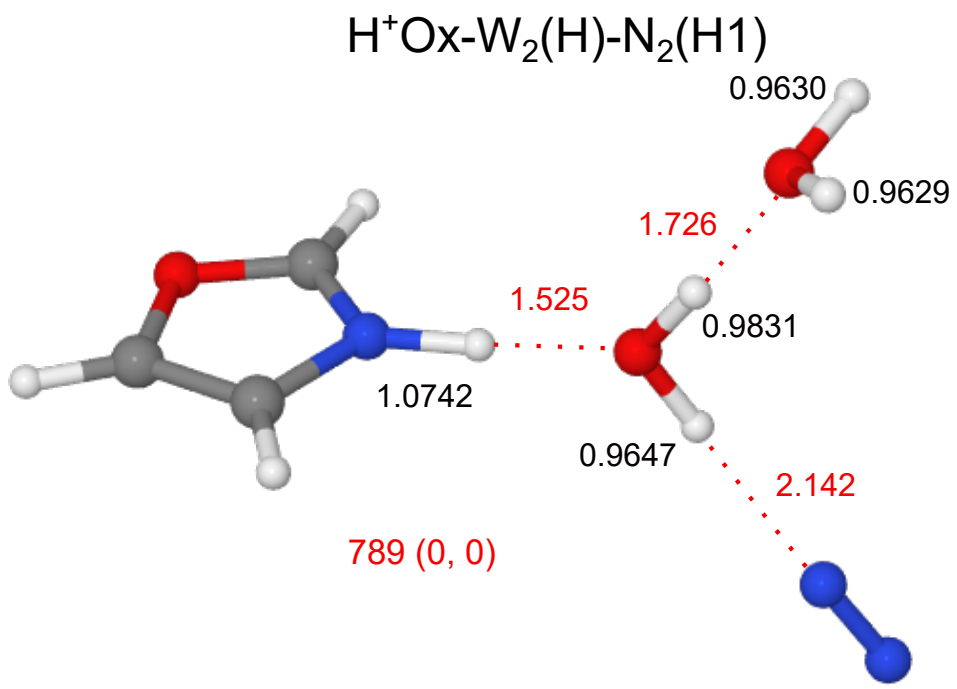
H+Ox-W2(H)-N2(H1)
0.9630
0.9629
1.726
1.525
0.9831
1.0742
0.9647
2.142
789 (0, 0)

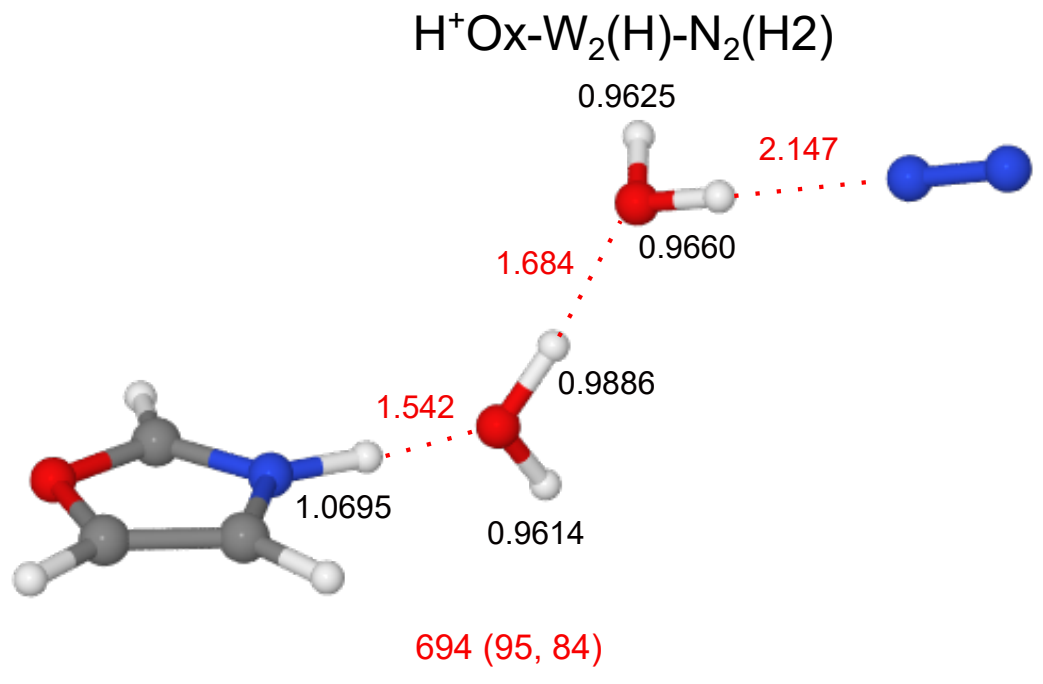
H+Ox-W2(H)-N2(H2)
0.9625
2.147
0.9660
1.684
0.9886
1.542
1.0695
0.9614
694 (95, 84)

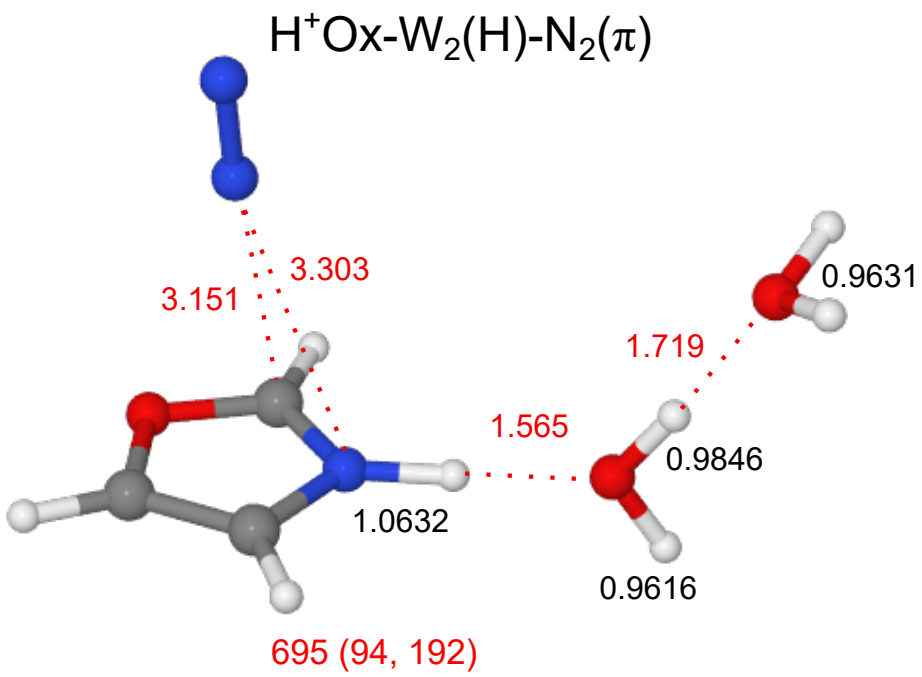
H+Ox-W2(H)-N2(π)
3.303
3.151
0.9631
1.719
1.565
0.9846
1.0632
0.9616
695 (94, 192)

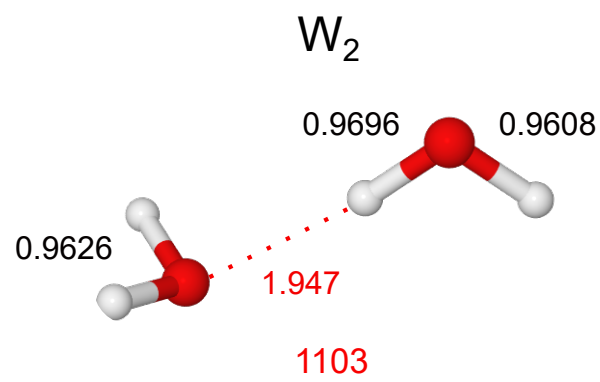
W2
0.9696
0.9608
0.9626
1.947
1103

Figure 4

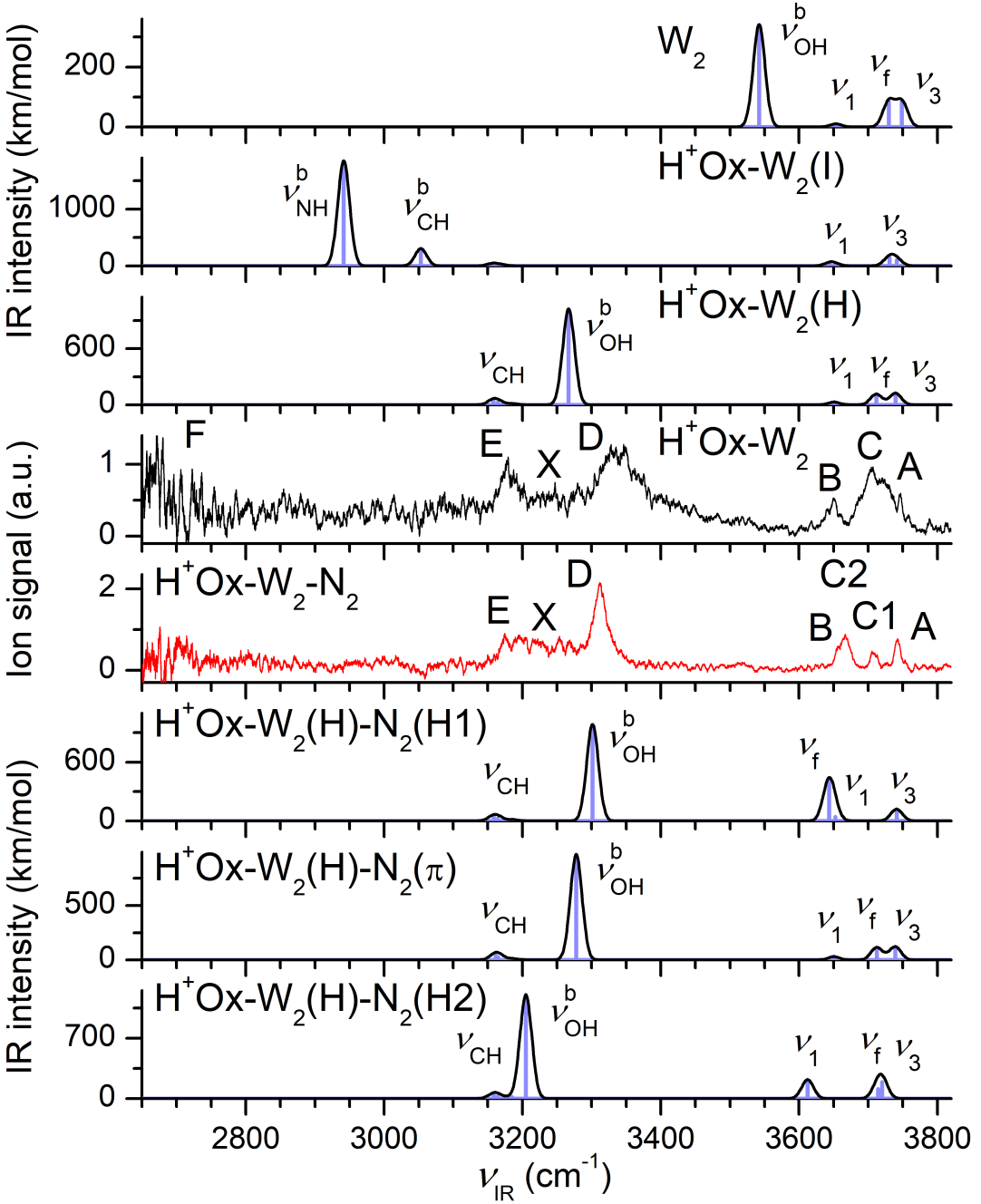
IR intensity (km/mol)
Ion signal (a.u.)
IR intensity (km/mol)
W2
H+Ox-W2(I)
H+Ox-W2(H)
H+Ox-W2
H+Ox-W2-N2
H+Ox-W2(H)-N2(H1)
H+Ox-W2(H)-N2(π)
H+Ox-W2(H)-N2(H2)
νb OH
νb NH
νb CH
νCH
νf
ν1
ν3
F
E
X
D
C
B
A
C2
C1
2800
3000
3200
3400
3600
3800
νIR (cm-1)

Figure 5

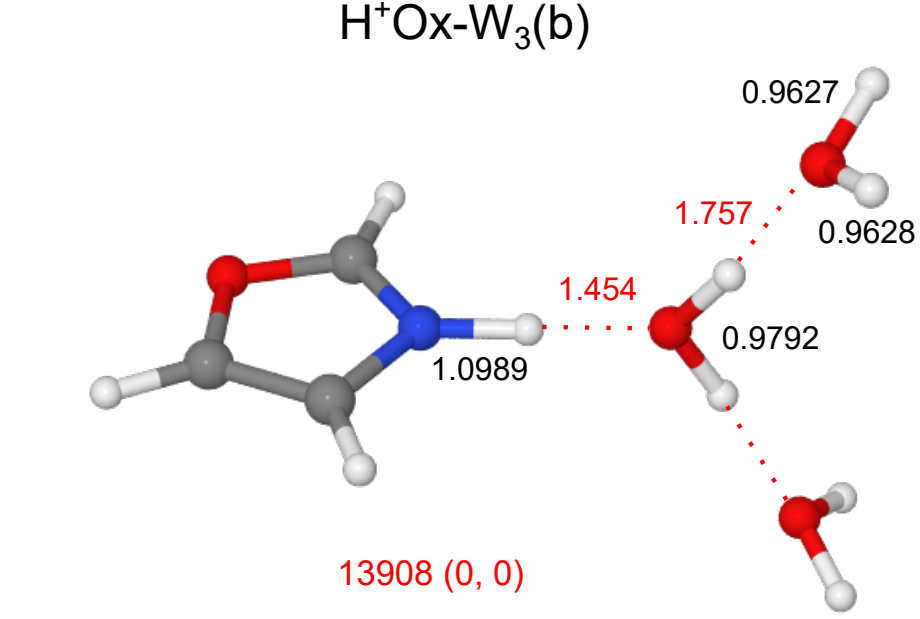
H+Ox-W3(b)
0.9627
1.757
0.9628
1.454
0.9792
1.0989
13908 (0, 0)

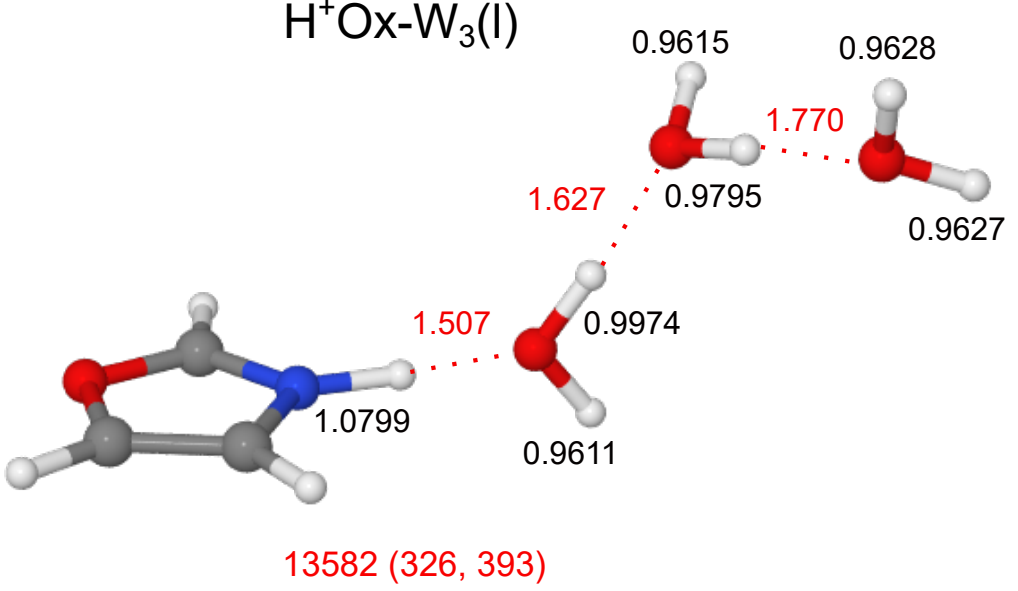
H+Ox-W3(l)
0.9615
0.9628
1.770
1.627
0.9795
0.9627
1.507
0.9974
1.0799
0.9611
13582 (326, 393)

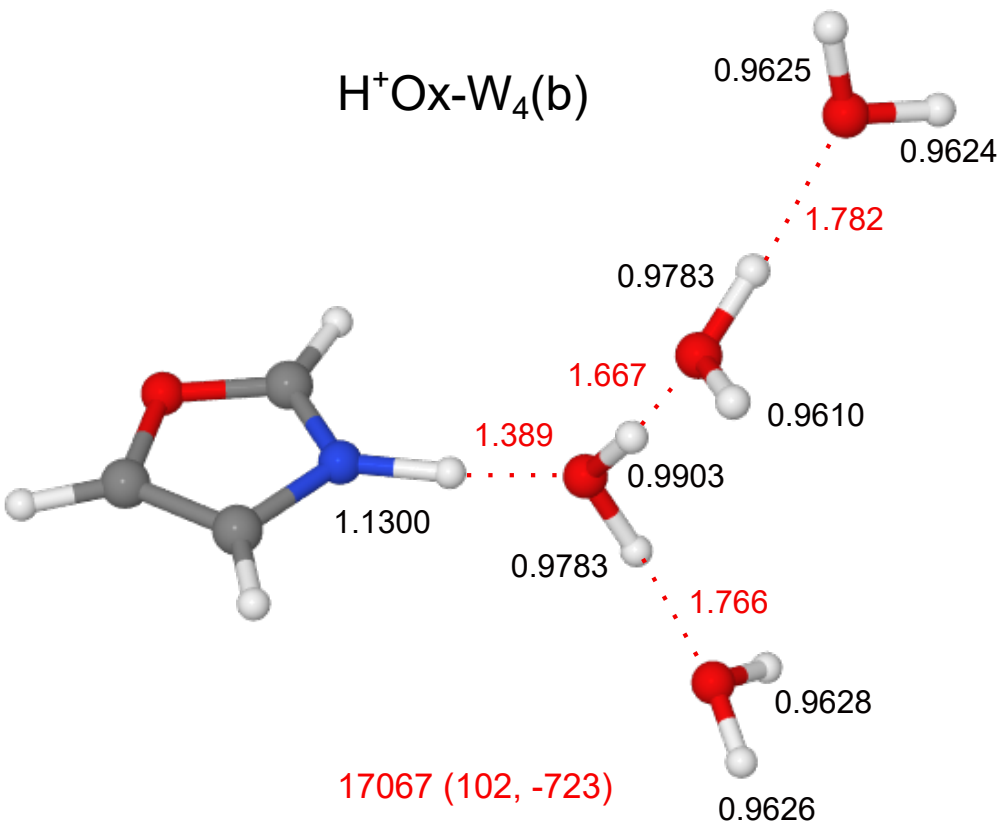
H+Ox-W4(b)
0.9625
0.9624
1.782
0.9783
1.667
0.9610
1.389
0.9903
1.1300
0.9783
1.766
0.9628
17067 (102, -723)
0.9626

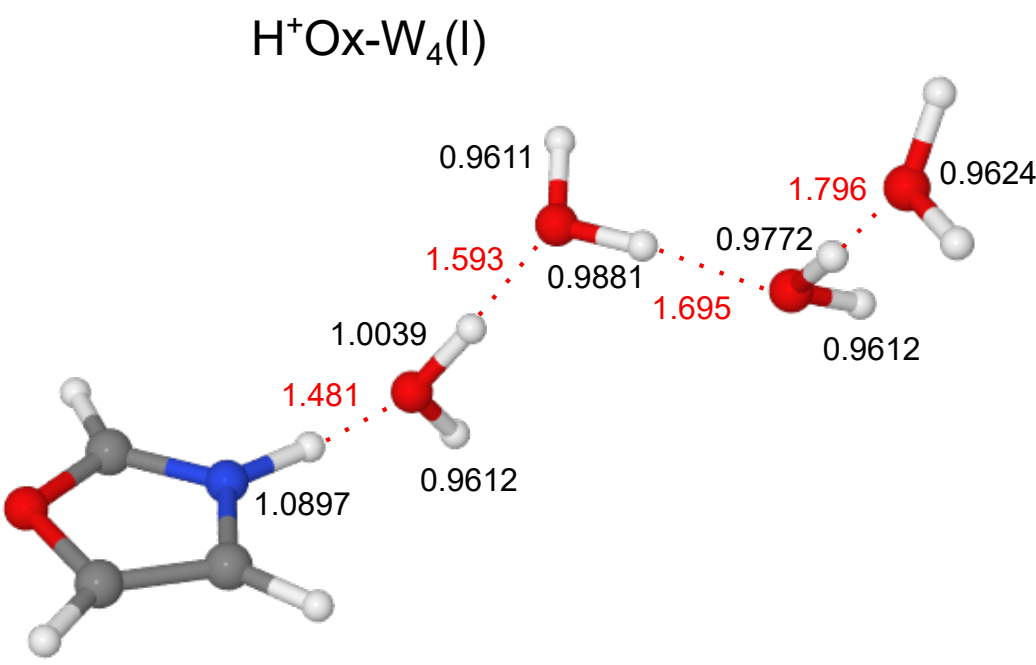
H+Ox-W4(l)
0.9611
0.9624
1.796
0.9772
1.593
0.9881
1.695
0.9612
1.0039
1.481
0.9612
1.0897
16425 (744, -96)

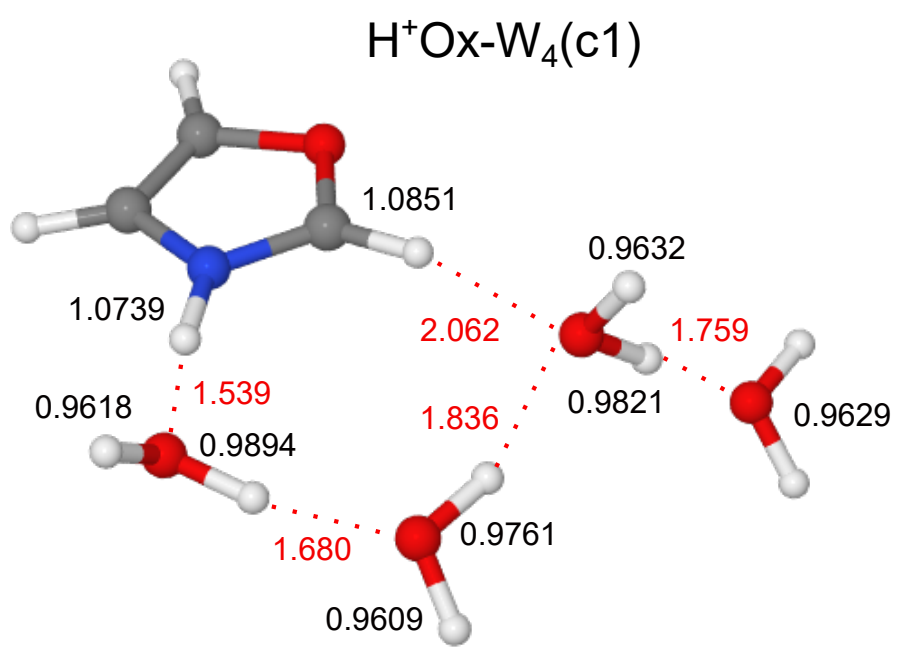
H+Ox-W4(c1)
1.0851
1.0739
0.9632
2.062
1.759
0.9821
0.9629
0.9618
1.539
0.9894
1.836
1.680
0.9761
0.9609
17169 (0, 0)

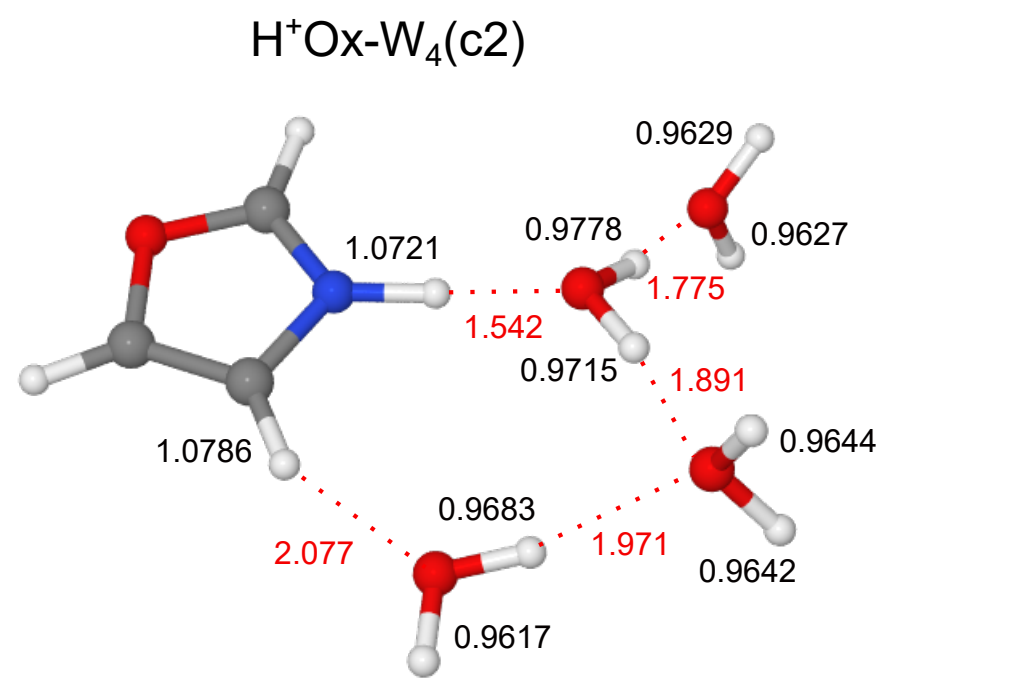
H+Ox-W4(c2)
0.9629
0.9627
1.0721
0.9778
1.775
1.542
0.9715
1.891
0.9644
1.0786
0.9683
2.077
1.971
0.9642
0.9617
16495 (674, 344)

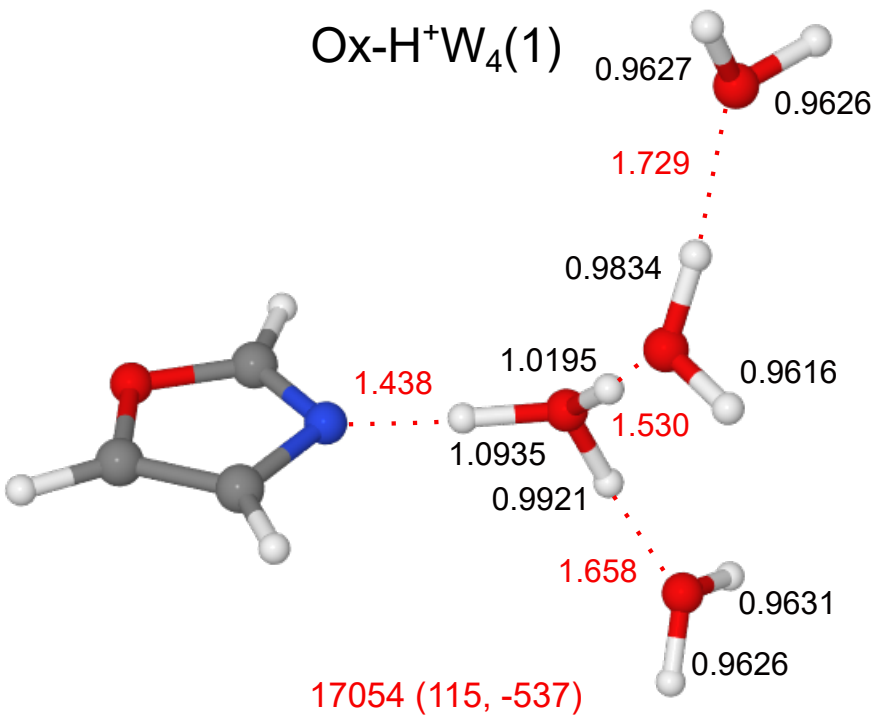
Ox-H+W4(1)
0.9627
0.9626
1.729
0.9834
1.438
1.0195
0.9616
1.530
1.0935
0.9921
1.658
0.9631
0.9626
17054 (115, -537)

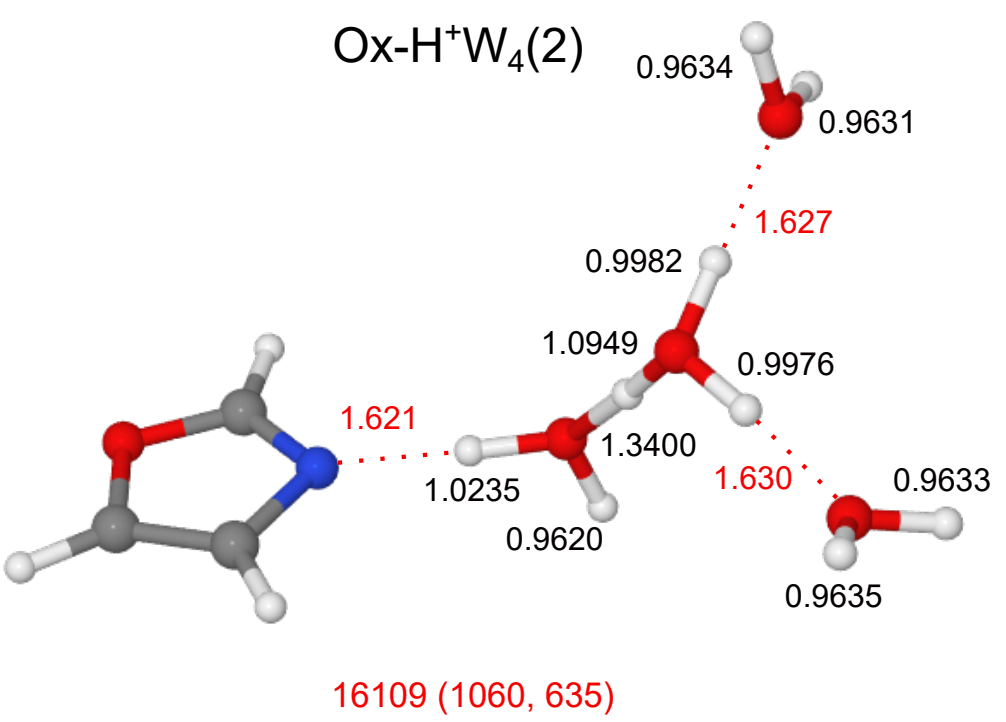
Ox-H+W4(2)
0.9634
0.9631
1.627
0.9982
1.0949
0.9976
1.621
1.3400
1.0235
1.630
0.9633
0.9620
0.9635
16109 (1060, 635)

Figure 6

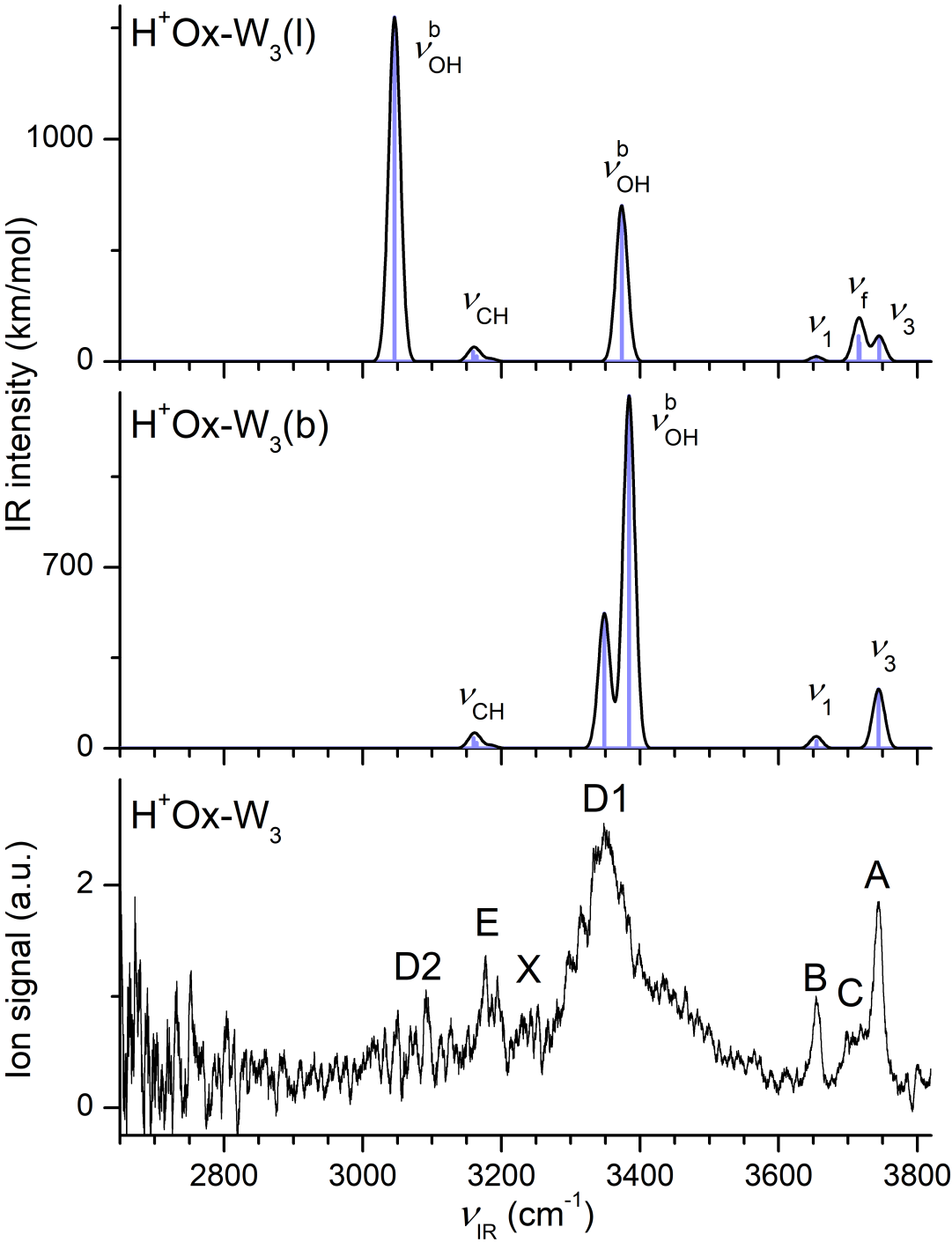
H+Ox-W3(I)
ν_{OH}^{b}
1000
ν_{OH}^{b}
ν_{CH}
ν_f
ν_1
ν_3
0
H+Ox-W3(b)
ν_{OH}^{b}
700
ν_3
ν_{CH}
ν_1
0
H+Ox-W3
D1
2
A
E
D2
X
B
C
0
IR intensity (km/mol)
Ion signal (a.u.)
2800
3000
3200
3400
3600
3800
ν_{IR} (cm-1)

Figure 7

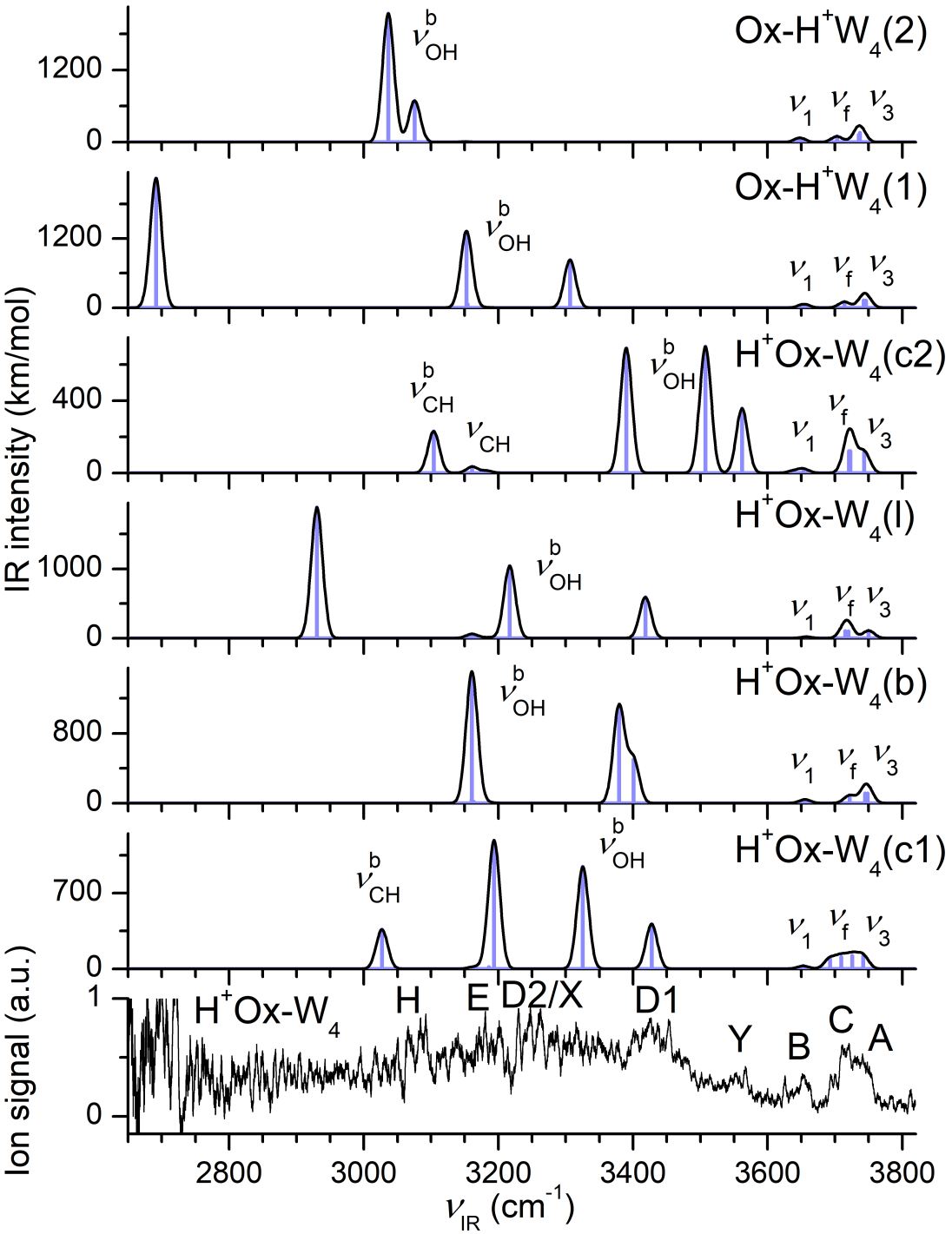
Ox-H+W4(2)
Ox-H+W4(1)
H+Ox-W4(c2)
H+Ox-W4(I)
H+Ox-W4(b)
H+Ox-W4(c1)
H+Ox-W4
IR intensity (km/mol)
Ion signal (a.u.)
νIR (cm-1)
H
E
D2/X
D1
Y
B
C
A

Figure 8

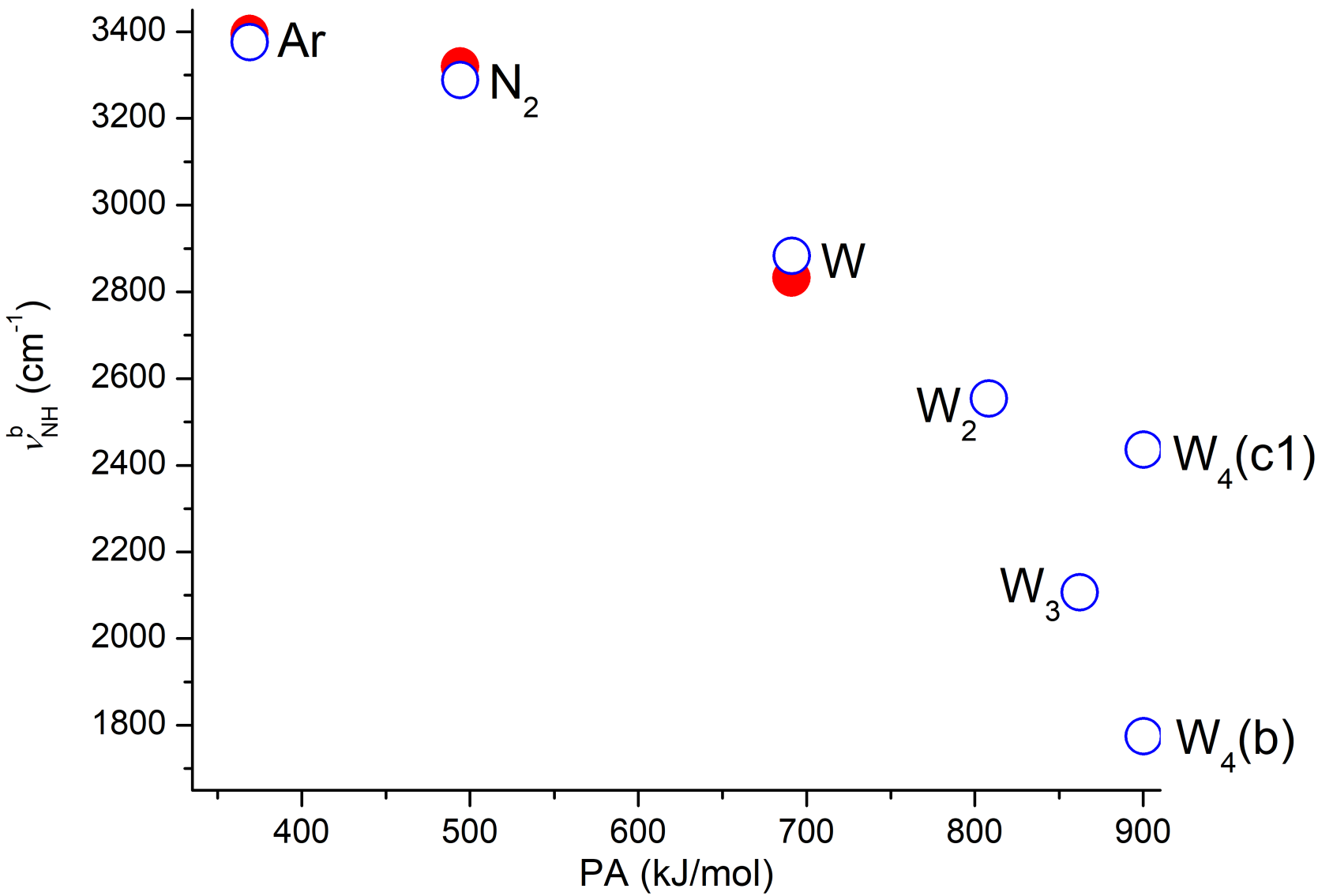
3400
3200
3000
2800
2600
2400
2200
2000
1800
ν^{b}_{NH} (cm^{-1})
400
500
600
700
800
900
PA (kJ/mol)
Ar
N_2
W
W_2
W_4(c1)
W_3
W_4(b)

Figure 9

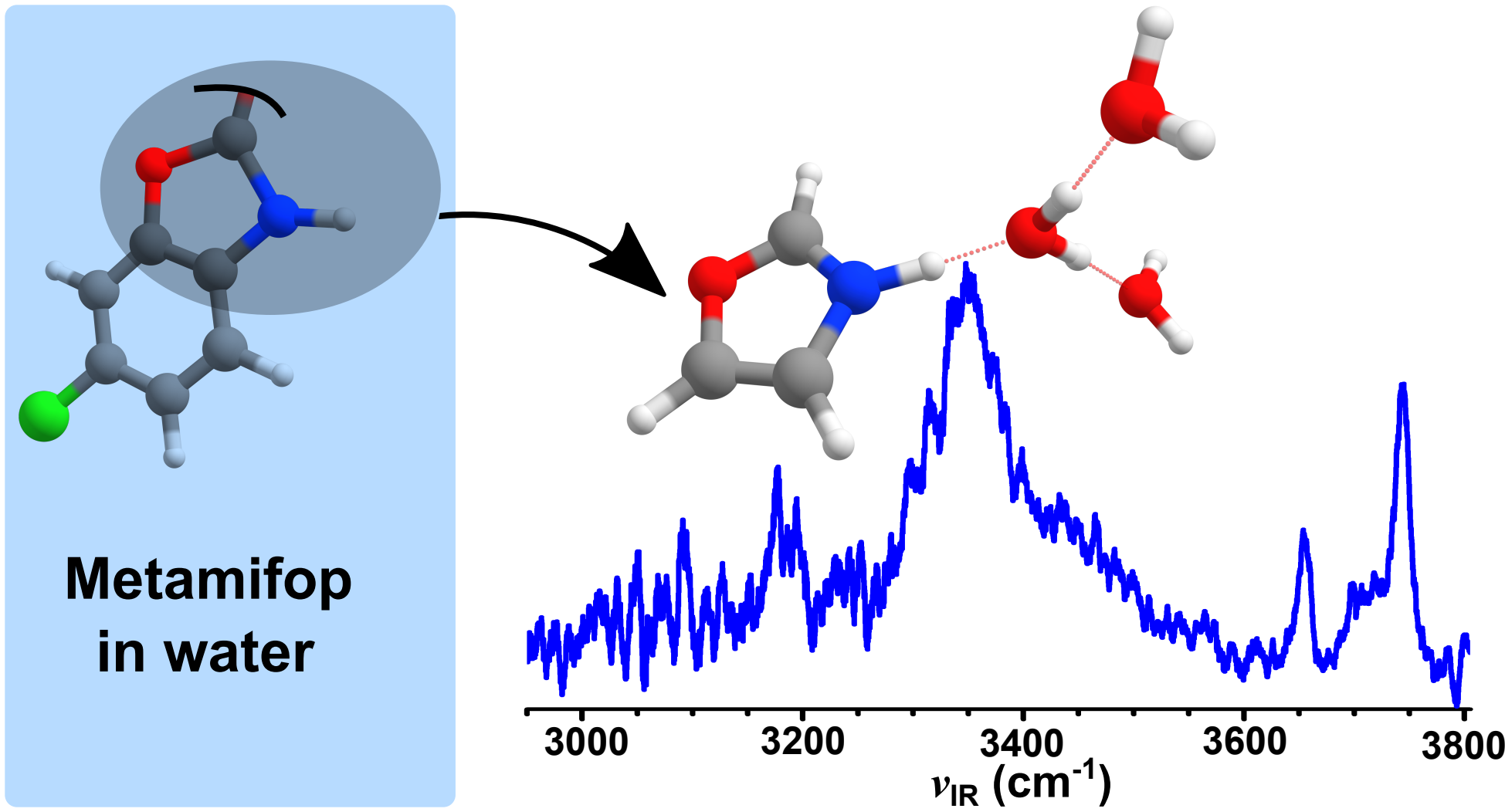
Metamifop
in water
3000
3200
3400
3600
3800
ν_{IR} (cm^{-1})

Supporting Information

Microhydration Structures of Protonated Oxazole

Kuntal Chatterjee and Otto Dopfer*

Institut für Optik und Atomare Physik, TU Berlin, Hardenbergstr. 36, 10623 Berlin, Germany

* Corresponding author: dopfer@physik.tu-berlin.de

Figure Captions

Figure S1. Optimized structure of the neutral Ox-W dimer and its linear IR absorption spectrum calculated at the B3LYP-D3/aug-cc-pVTZ level. Binding energy (D_0) and bond lengths are given in cm^{-1} and Å, respectively.

Figure S2. NBO atomic charge distribution (in e) of selected $H^+Ox\text{-}W_{n\leq4}$ structures obtained at the B3LYP-D3/aug-cc-pVTZ level.

Figure S3. Potential energy barrier (E_e) for internal rotation of the W ligand in $H^+Ox\text{-}W(H)$ calculated at the B3LYP-D3/aug-cc-pVTZ level in cm^{-1}. Bond lengths are given in Å.

Figure S4. Optimized structure and linear IR absorption spectrum of the $H^+Ox\text{-}W(C5)$ isomer calculated at the B3LYP-D3/aug-cc-pVTZ level. Binding energy (D_0) and bond lengths are given in cm^{-1} and Å, respectively. Numbers in parentheses correspond to relative energies and free energies (E_0, G_0) with respect to $H^+Ox\text{-}W(H)$ in cm^{-1}.

Figure S5. Potential energy barrier (E_e) between $H^+Ox\text{-}W_4(b)$ and $Ox\text{-}H^+W_4(1)$ evaluated at the B3LYP-D3/aug-cc-pVTZ level in cm^{-1}.

Figure S6. Orbital interaction between the σ* orbital of the X-H bond (X=N/O/C) and the lone pair of O involved in the XH…O H-bonds of selected $H^+Ox\text{-}W_{n\leq4}$ isomers obtained from the NBO analysis at the B3LYP-D3/aug-cc-pVTZ level. $E^{(2)}$ values given in kJ/mol.

Figure S7. Visualization of the NCI analysis of the XH…O (X=N/O/C) H-bonds in selected $H^+Ox\text{-}W_{n\leq4}$ isomers calculated at the B3LYP-D3/aug-cc-pVTZ level. ρ* values for the H-bonds are given in a.u.

Figure S8. Experimental proton affinities of W_n clusters (n=1-4) and Ox.

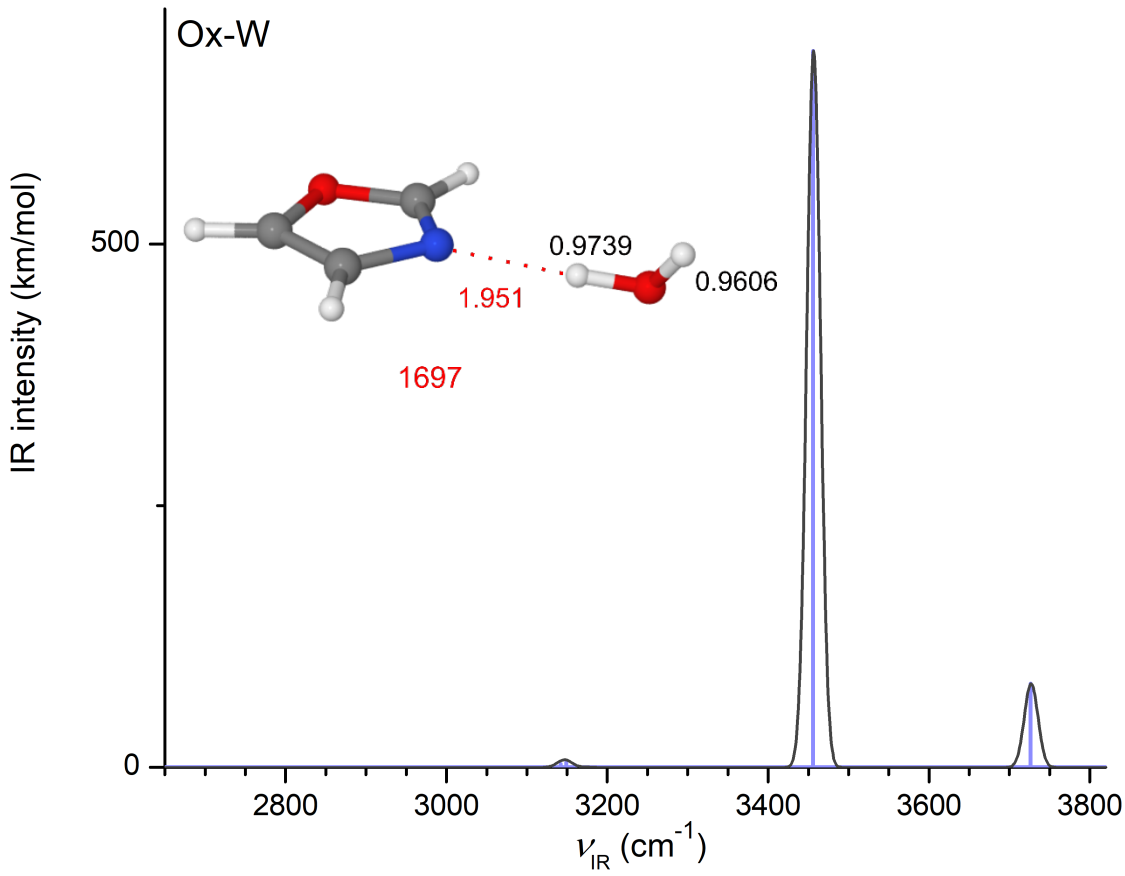
Ox-W
IR intensity (km/mol)
500
0
0.9739
0.9606
1.951
1697
2800
3000
3200
3400
3600
3800
ν_{IR} (cm^{-1})

Figure S1

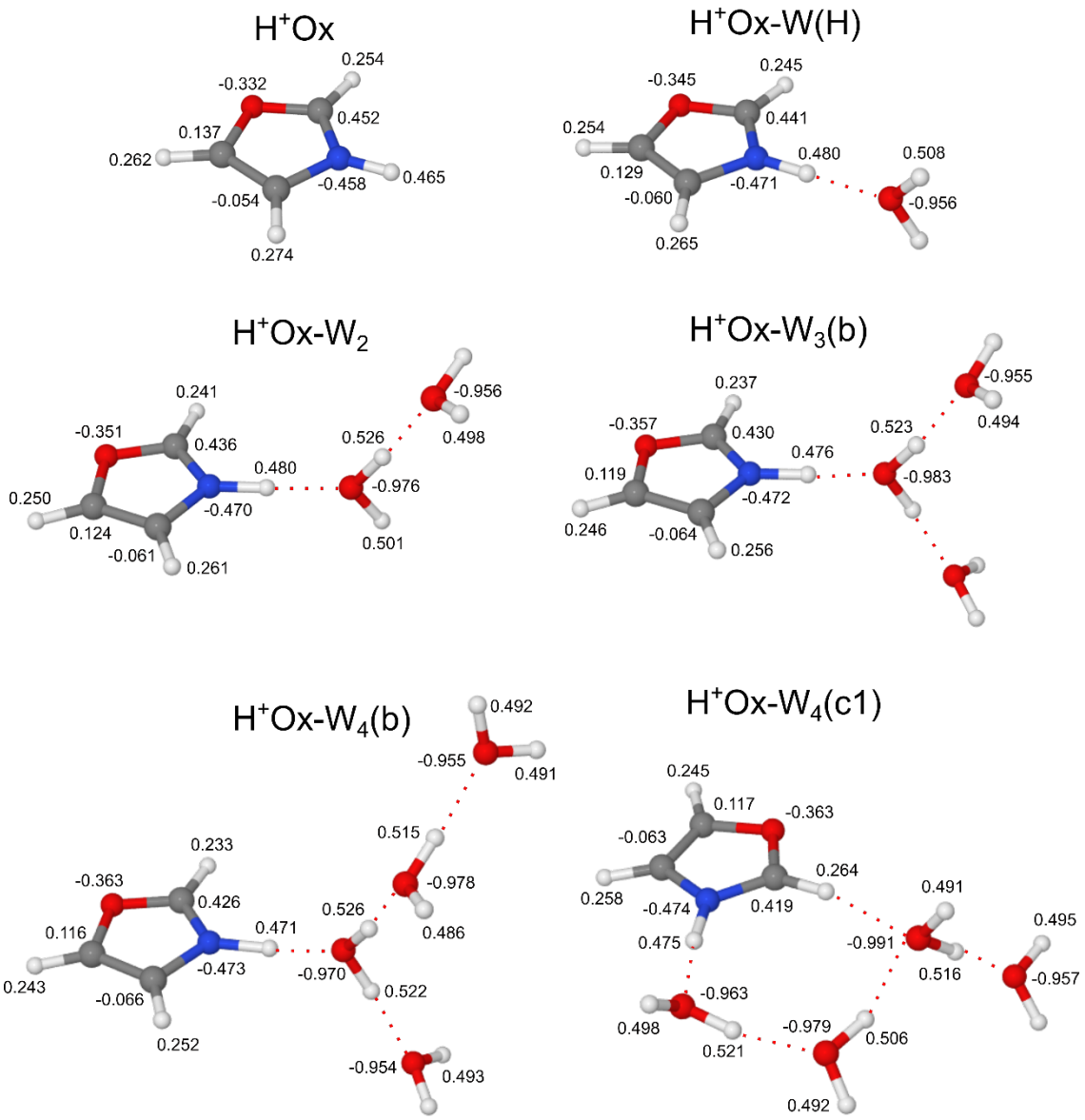
H+Ox
0.254
-0.332
0.452
0.137
0.262
0.465
-0.458
-0.054
0.274
H+Ox-W(H)
0.245
-0.345
0.441
0.254
0.480
0.508
0.129
-0.471
-0.060
-0.956
0.265
H+Ox-W2
0.241
-0.956
-0.351
0.436
0.526
0.498
0.480
-0.976
0.250
-0.470
0.124
0.501
-0.061
0.261
H+Ox-W3(b)
0.237
-0.955
-0.357
0.430
0.523
0.494
0.476
0.119
-0.983
-0.472
0.246
-0.064
0.256
H+Ox-W4(b)
0.492
-0.955
0.491
0.515
0.233
-0.978
-0.363
0.426
0.526
0.471
0.116
0.486
-0.473
-0.970
0.243
0.522
-0.066
0.252
-0.954
0.493
H+Ox-W4(c1)
0.245
0.117
-0.363
-0.063
0.264
0.491
0.258
-0.474
0.419
0.495
0.475
-0.991
0.516
-0.957
-0.963
0.498
-0.979
0.506
0.521
0.492

Figure S2

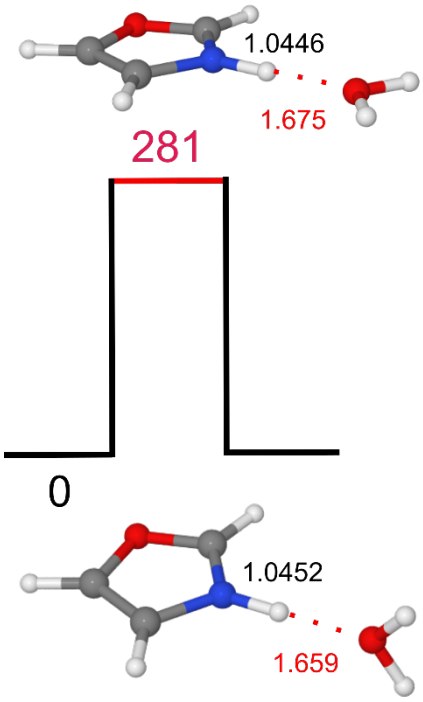

Figure S3

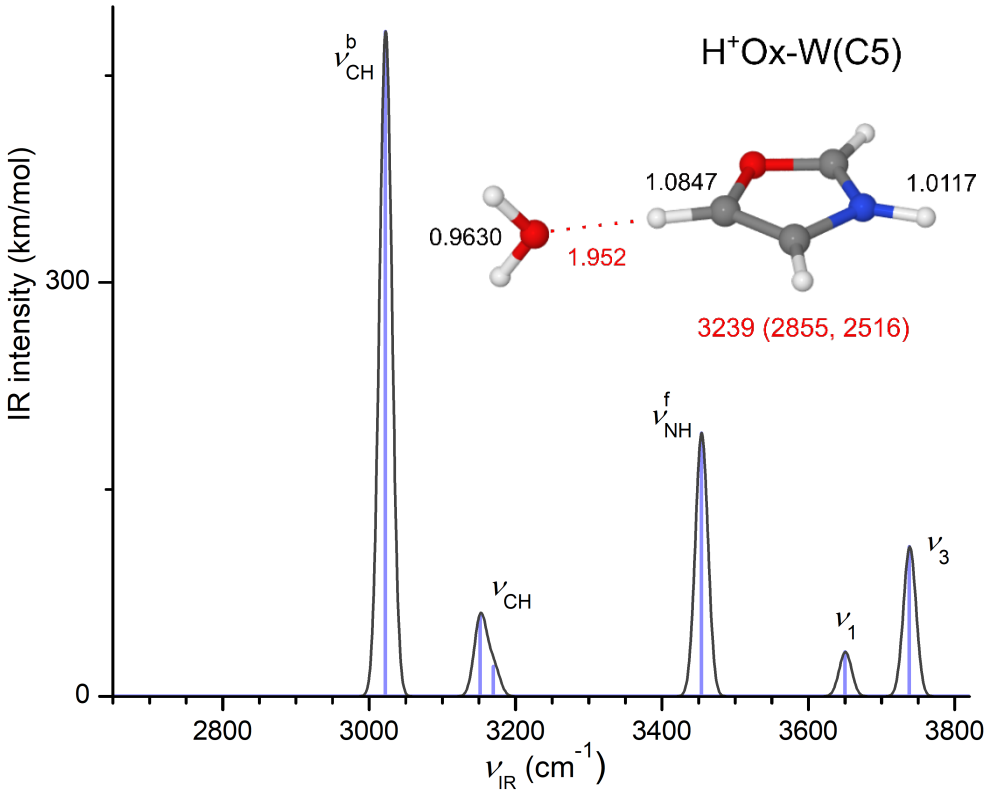
H+Ox-W(C5)
IR intensity (km/mol)
300
0
2800
3000
3200
3400
3600
3800
νIR (cm-1)
νbCH
νCH
νfNH
ν1
ν3
0.9630
1.952
1.0847
1.0117
3239 (2855, 2516)

Figure S4

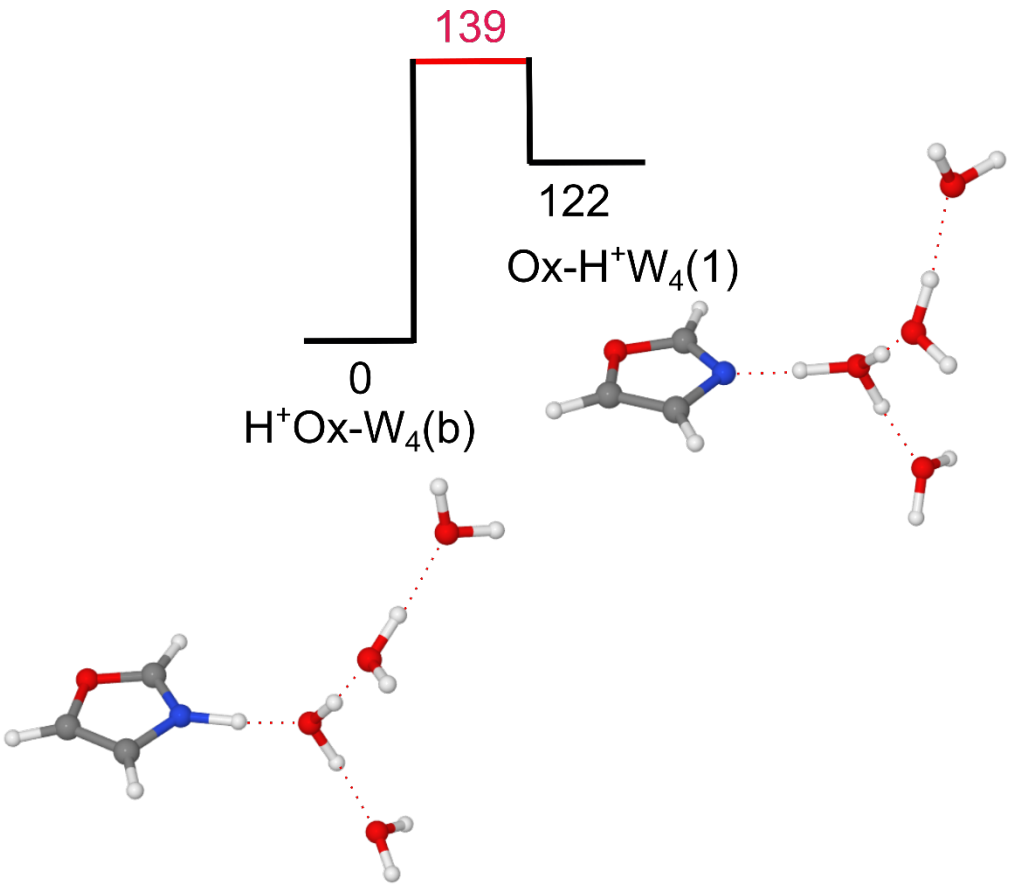

Figure S5

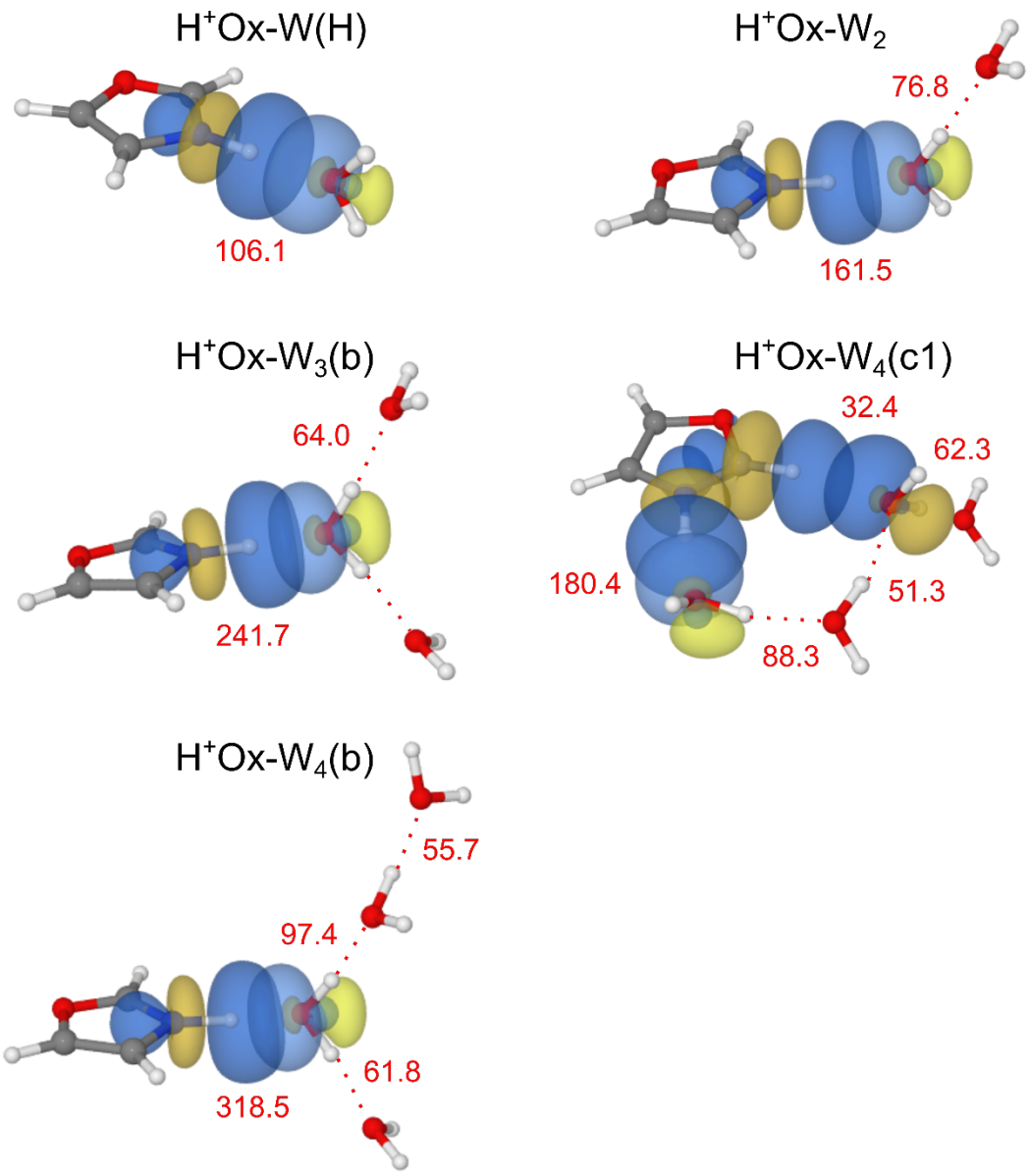
H+Ox-W(H)
106.1
H+Ox-W2
76.8
161.5
H+Ox-W3(b)
64.0
241.7
H+Ox-W4(c1)
32.4
62.3
180.4
51.3
88.3
H+Ox-W4(b)
55.7
97.4
61.8
318.5

Figure S6

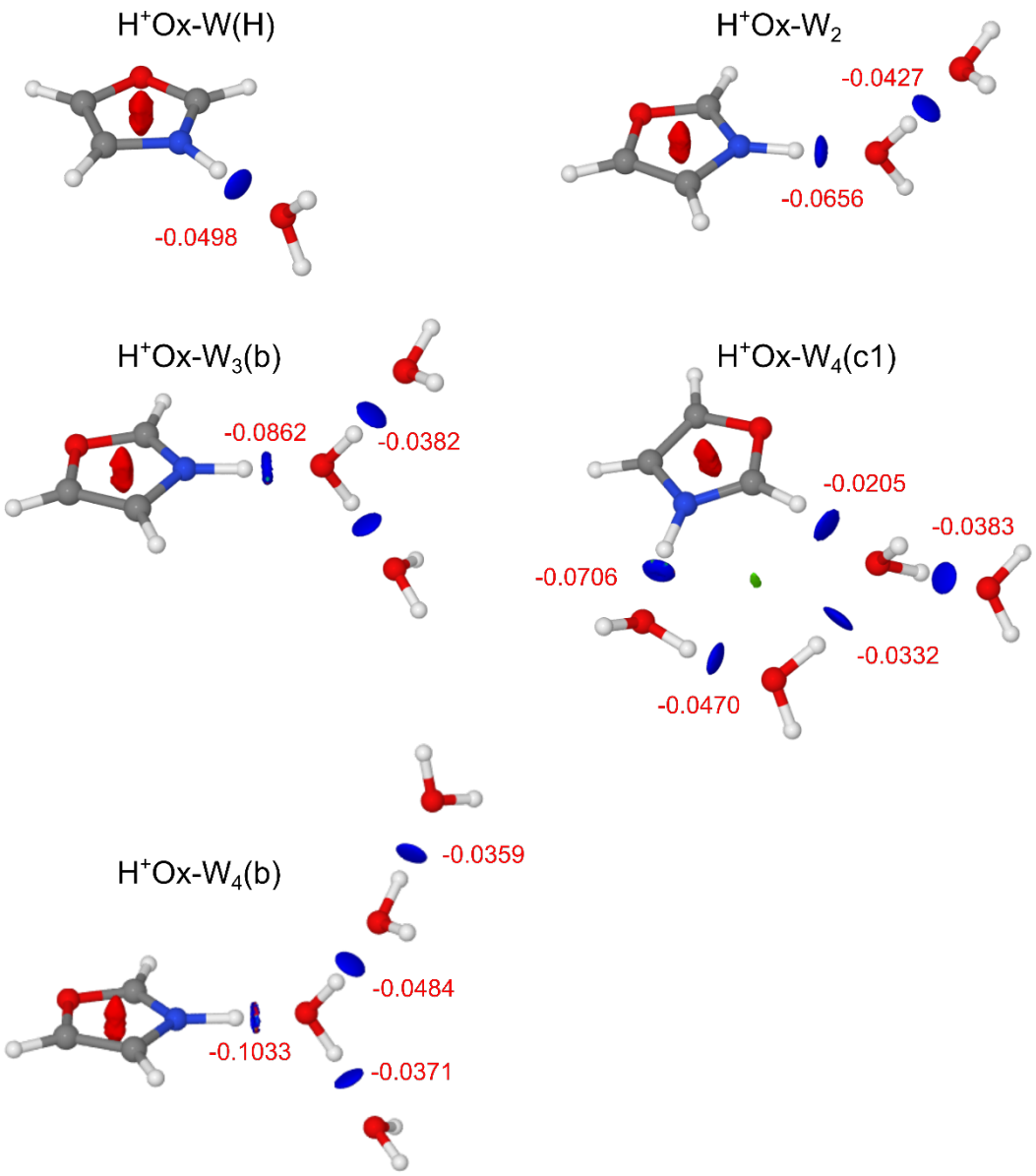
H+Ox-W(H)
-0.0498
H+Ox-W2
-0.0427
-0.0656
H+Ox-W3(b)
-0.0862
-0.0382
H+Ox-W4(c1)
-0.0205
-0.0383
-0.0706
-0.0332
-0.0470
H+Ox-W4(b)
-0.0359
-0.0484
-0.1033
-0.0371

Figure S7

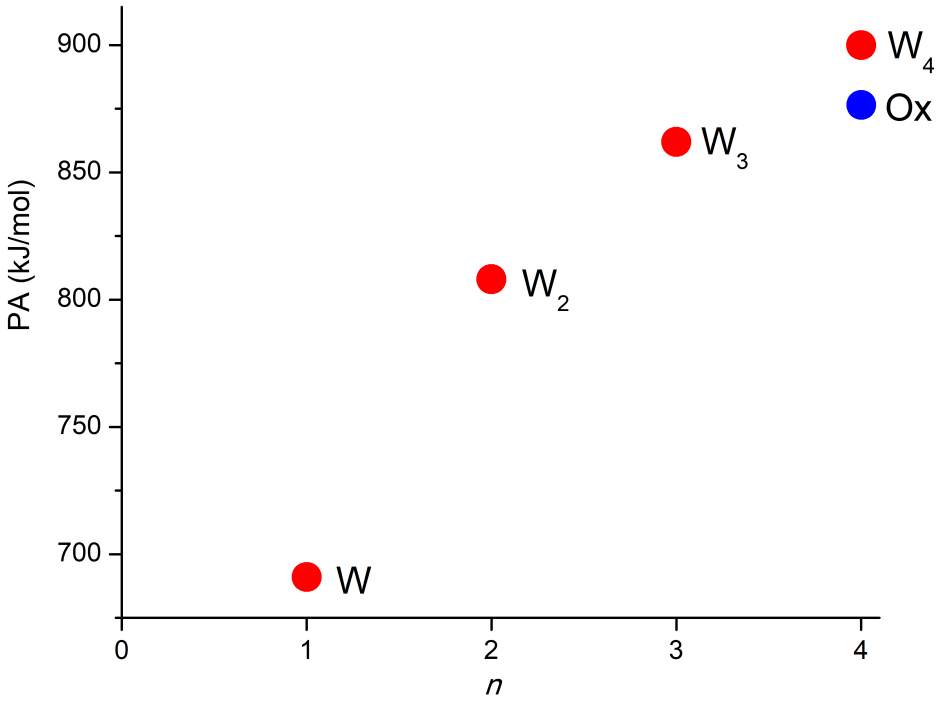

Figure S8